eTransportation 21 (2024) 100340

Contents lists available at ScienceDirect

eTransportation

journal homepage: www.journals.elsevier.com/etransportation

Thermodynamic and kinetic degradation of LTO batteries: Impact of different SOC intervals and discharge voltages in electric train applications

Haoze Chen [a,b,c,d], Ahmed Chahbaz [b,c,d], Sijia Yang [a,b,c,d,*], Weige Zhang [a], Dirk Uwe Sauer [b,c,d,e], Weihan Li [b,c,d,**]

[a] National Active Distribution Network Technology Research Center (NANTEC), Beijing Jiaotong University, No.3 Shangyuancun, Beijing, 100044, China
[b] Chair for Electrochemical Energy Conversion and Storage Systems, Institute for Power Electronics and Electrical Drives (ISEA), RWTH Aachen University, Campus-Boulevard 89, Aachen, 52074, Germany
[c] Center for Ageing, Reliability and Lifetime Prediction of Electrochemical and Power Electronic Systems, RWTH Aachen University, Campus-Boulevard 89, Aachen, 52074, Germany
[d] Jülich Aachen Research Alliance, JARA-Energy, Templergraben 55, Aachen, 52056, Germany
[e] Helmholtz Institute Münster (HI MS), IEK-12, Forschungszentrum Jülich, 52425, Jülich, Germany

ARTICLE INFO

Keywords:
Lithium-ion battery
Aging
$Li_4Ti_5O_{12}$
Electrochemical impedance spectroscopy
Differential voltage analysis

ABSTRACT

Lithium-titanate-oxide (LTO) based lithium-ion batteries show promise for longer lifespan, higher power capability, and lower life cycle cost for energy storage and electric transportation applications than graphite-based counterparts. However, the degradation mechanisms of LTO-based cells in the high and low state-of-charge (SOC) intervals and different discharge cut-off voltages are not clearly investigated. In this study, the application-related lifetime performance of high-power $Li_4Ti_5O_{12}$/$LiCoO_2$ batteries is investigated at five independent SOC intervals with 20 % depth-of-discharge (DOD) and three discharge cut-off voltages. Our results show that degradation increases significantly when the batteries are cycled within lower SOC intervals or with lower cut-off voltages. Additionally, thermodynamic degradation is more significant when cycled at 20 % DOD, while kinetic degradation dominates at 100 % DOD. For thermodynamic degradation, the determining degradation mode is shown to be the loss of active material in the negative electrode, while the active material loss at the cathode has a greater impact on the equilibrium voltage curve. The kinetic degradation is mainly due to the slower charge transfer process and diffusion process at the cathode, which increases polarization impedance.

1. Introduction

Due to energy depletion and environmental demands, lithium-ion batteries are being widely adopted across various fields due to their exceptional performance and numerous advantages [1,2]. Among them, lithium titanate oxide (LTO) based batteries stand out as an ideal choice for electric transportation systems thanks to their outstanding power capabilities, enhanced safety features, and excellent temperature adaptability [3–5]. However, during long-term service, the LTO batteries inevitably undergo aging, which is highly dependent on the application scenarios. Different usage conditions can lead to distinct degradation modes in LTO batteries, resulting in varying impacts on their performance [6,7]. In some scenarios, the performance of LTO batteries may remain relatively stable, while in other situations, performance degradation can occur, potentially leading to system failure or even triggering thermal runaway [8]. Therefore, it is crucial to consider the aging behavior of LTO batteries under various conditions when designing electric transportation systems.

According to the usage conditions, the stress factors that affect the aging behavior of Lithium-ion batteries include charge/discharge current rate (C-rate), charge/discharge cut-off voltage, depth of discharge (DOD), and ambient temperature [9]. Recently, several studies have been conducted to investigate the degradation of LTO batteries under these stress factors.

* Corresponding author. National Active Distribution Network Technology Research Center (NANTEC), Beijing Jiaotong University, No.3 Shangyuancun, Beijing, 100044, China.
** Corresponding author. Chair for Electrochemical Energy Conversion and Storage Systems, Institute for Power Electronics and Electrical Drives (ISEA), RWTH Aachen University, Campus-Boulevard 89, Aachen, 52074, Germany.
E-mail addresses: sjyang@bjtu.edu.cn (S. Yang), weihan.li@isea.rwth-aachen.de (W. Li).

https://doi.org/10.1016/j.etran.2024.100340
Received 6 August 2023; Received in revised form 16 May 2024; Accepted 19 May 2024
Available online 21 May 2024

Bank et al. investigated the life performance at elevated temperatures over various C-rates and DODs [10,11]. The results showed that the C-rate had a negligible effect on cycle life, while only DOD higher than 70 % would significantly increase battery degradation. In addition, the cells showed no significant additional degradation caused by temperatures below 60 °C, while the sharp degradation exhibited at 80 °C could be attributed to the gas-producing behavior triggering structural damage to the electrodes. This is consistent with the findings of Zhang et al. [12] and Devie et al. [13,14].

Liu et al. analyzed the cyclic aging of the batteries at different C-rates under room temperature [15]. The result showed that batteries cycled at lower C-rates exhibit larger capacity degradation. They attributed this phenomenon to the smaller DOD at higher C-rates due to charge/discharge cut-off voltage limitations. This is consistent with our previous study that increasing the C-rate from 1C to 3C does not have a significant impact on the battery, whereas expanding the DOD from 90 % to 100 % leads to a rapid decline in capacity [6].

Dubarry et al. investigated the durability and reliability of LTO batteries under electric utility grid operation [16]. The results showed that cyclic aging using representative current profiles as grid utility storage system operation was more pronounced for higher C-rates, smaller SOC intervals, and higher temperatures. Furthermore, Baure et al. investigated the new generation of LTO batteries from the same manufacturer to forecast the aging behavior under different grid application usage [17]. The lifetime forecast shows an accelerated capacity loss after only six years of deployment for batteries tested at 35 °C and low SOC. Under all other conditions, the capacity loss is less than 20 % if temperatures remain below 35 °C, enabling a 20-year deployment life.

These research results indicate that the DOD has a significant and noticeable effect on the lifespan of the LTO battery, while the C-rate and temperature have a minor effect. However, most of the studies have overlapping regions between different DODs, which prevents them from decoupling and analyzing their independent effects. Therefore, this paper divides the 0–100 % SOC interval into five equal-sized parts without overlapping each other (0–20 %, 20–40 %, 40–60 %, 60–80 %, and 80–100 %). There are several advantages of dividing the intervals in this way: (a) Since the DODs are the same, it is easy to compare the different parts to find the optimal working interval for 20 % DOD operating scenarios in hybrid rail-transit applications [5,18–20]. (b) The battery degradation in different SOC intervals can be analyzed independently, as no overlapping parts exist. (c) It is more convenient to analyze the relationship between the small interval (20 % DOD) and the large interval (100 % DOD) due to the fact that the large interval can be obtained from the superposition of the small intervals. Furthermore, our previous studies have validated the effectiveness of this division method on graphite cells [21]. In the future, we will compare and analyze the difference in cyclic aging between graphite cells and LTO cells at different SOC intervals.

In addition, the discharge cut-off voltage is also an important factor affecting the performance of the LTO battery. In practical applications, the discharge cut-off voltage is often used to estimate the maximum available energy and power of the battery [22–25]. Higher discharge cut-off voltage results in lower energy and power output. However, if the discharge cut-off voltage is too low to cause over-discharge, it will result in a rapid decrease in LTO battery capacity [26]. Therefore, in order to solve the contradiction and seek the balance between energy and lifespan, the aging of LTO batteries under three different discharge cut-off voltages was also investigated.

The performance degradation of lithium-ion batteries after aging is primarily governed by their constituent electrode materials, whose changes in thermodynamic and kinetic properties are considered to be the determining factor [27]. The thermodynamic properties include attributes related to battery capacity (e.g. loss of Li inventory "LLI," loss of active material in the cathode "LAM_{cat}," or in the anode "LAM_{an}") and attributes related to the equilibrium potential of the cell [28–30]. On the other hand, the kinetic properties include the rates of ion diffusion and charge transfer processes, which are mainly expressed as the magnitude of the polarization impedance of the battery [31,32]. In order to investigate the degradation of thermodynamic and kinetic properties under different aging conditions, the following approaches have been used in this paper: First, we investigate the thermodynamic degradation under different cycle conditions by combining the differential voltage analysis (DVA) with the open circuit voltage (OCV) reconstruction method. Then, the kinetic degradation under different aging conditions was compared by analyzing the change in impedance, and furthermore, electrochemical impedance spectroscopy (EIS) and distribution of relaxation time (DRT) analysis were used to determine the mechanism of degradation. An equivalent circuit model is also developed to verify the accuracy of the DRT analysis.

The overall workflow of our research is given in Fig. 1. Research in this paper is beneficial for optimizing the battery operating range to prolong the battery lifetime, ultimately reducing life cycle costs in electric transportation systems. The results can also determine the optimal discharge cut-off voltage to achieve maximum available energy and power performance without compromising the battery lifespan.

2. Experimental

In this study, LTO-based pouch cells with lithium cobalt oxide (LCO) cathode and LTO anode were investigated. The nominal capacity of the battery is 25 Ah. The operational voltage range of the battery recommended by the manufacturer is 1.5 V–2.8 V.

2.1. Cyclic aging test

As shown in Fig. 2, the cyclic aging test was performed under eight conditions, including five different SOC intervals with 20 % DOD and three using different cut-off voltages. In this paper, the difference in discharge capacity under different cut-off voltages is less than 0.31 %, as shown in Fig. S2. In order to distinguish from the experiments at 20 % DOD, we consider that the three experiments at different discharge cut-off voltages have all reached their respective fully discharge state, i.e., 0 % SOC. That is, the three cells were cycled at 0–100 % SOC at 100 % DOD with different cut-off voltages. The capacity corresponding to 20 % DOD is based on the nominal capacity obtained in the reference performance test and is updated every 200 cycles.

Cycling was performed at a constant current (CC) rate of 4C (100 A) in charge and discharge direction with no rest time in between. However, for operation points reaching 100 % SOC, a constant-voltage (CV) phase was included after the CC charging process until the current reached a value below C/10 to ensure that the anode was fully lithiated. In addition, for the operating point reaching 0 % SOC, a two-stage 4C/1C CC discharge process is performed to ensure the battery is fully discharged.

The batteries were cycled using a multi-channel ARBIN LBT-5V-100 A battery testing system. Batteries were placed in a thermal chamber to maintain a constant ambient temperature of 25 °C. Additionally, in order to prevent different temperature rises during cycling under other conditions, each battery is equipped with heat sinks and fans to ensure that the battery temperature is nearly consistent with the chamber temperature during cycling. The surface temperature change of the battery is limited to ±3 °C. The specific experimental setup is described in Note S1, Supplementary material.

2.2. Reference performance test

The reference performance test includes a nominal capacity test, a quasi-stationary OCV test, and a hybrid pulse power characterization (HPPC) test. The applied current and voltage response of the RPT are shown in Fig. 3(a and b), respectively. Before the cyclic aging tests were started, we conducted an initial RPT on all specimens to obtain information on the pristine cell behavior. Afterward, the RPT was repeated

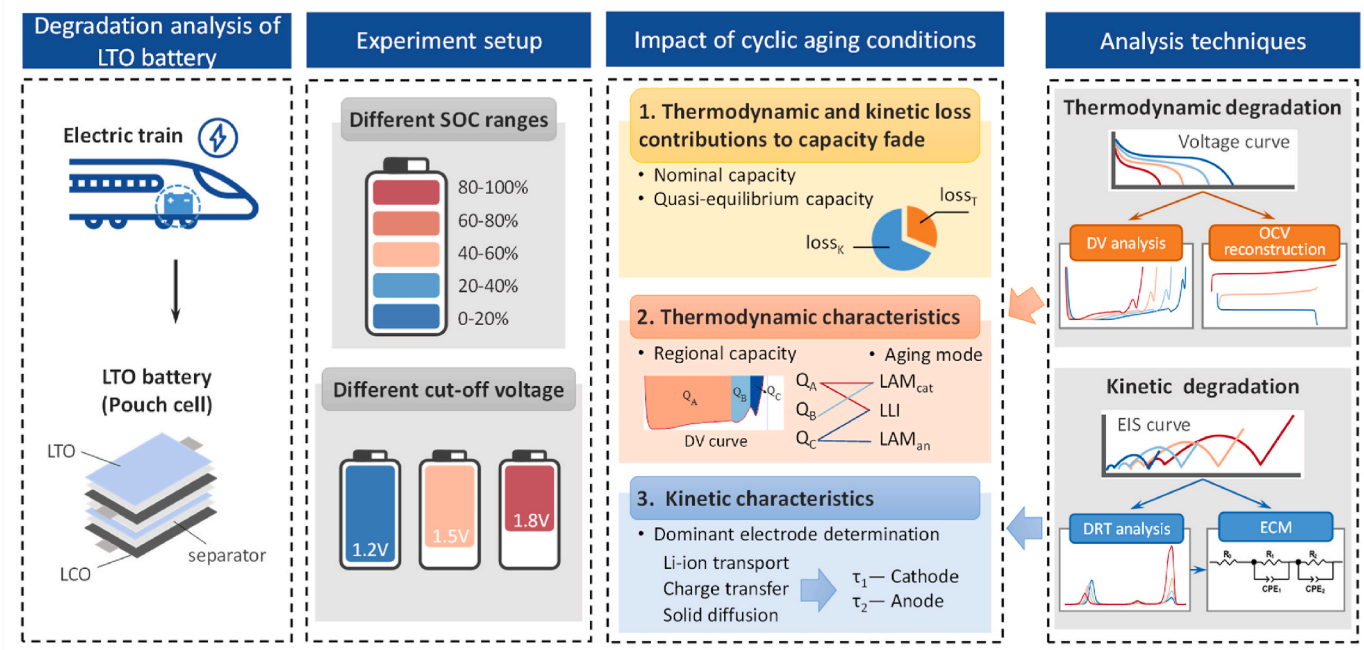

Fig. 1. Overall flow chart of analyzing the degradation of LTO batteries under different cyclic aging conditions.

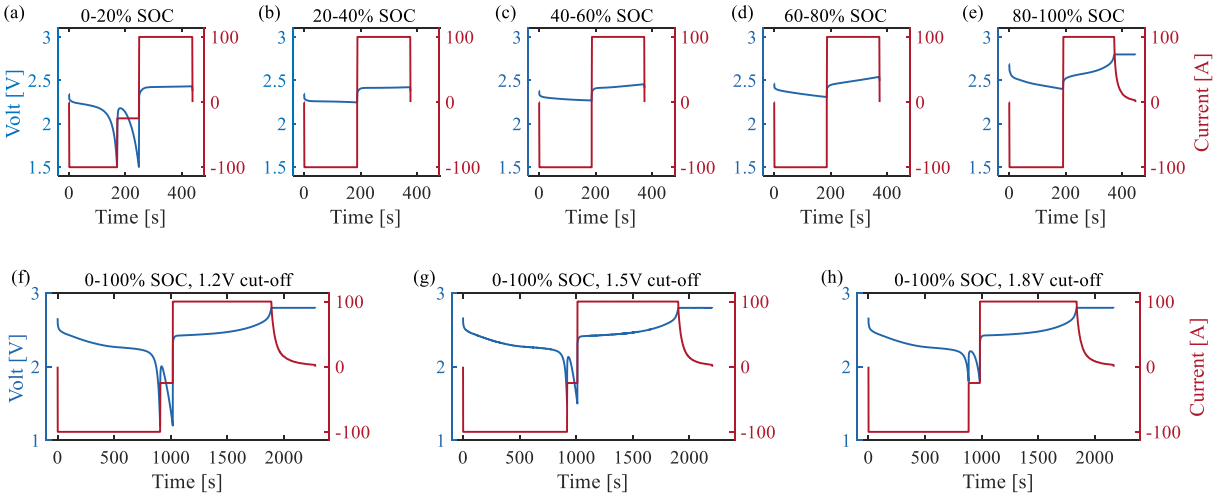

Fig. 2. Current and voltage response of one aging cycle under eight different conditions.

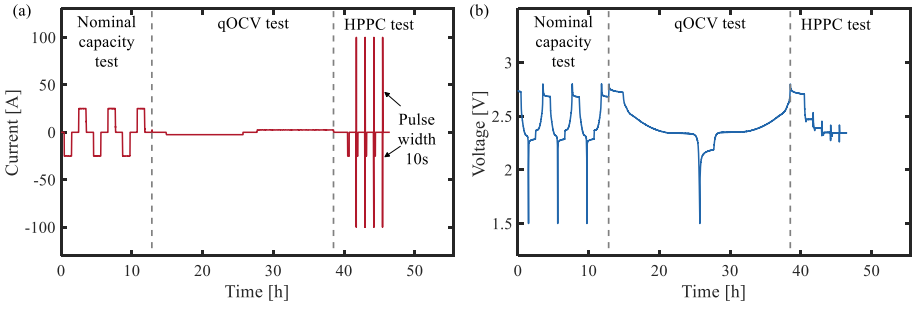

Fig. 3. The response of (a) current and (b) voltage during an RPT.

every 200 cycles.

The nominal capacity test, as recommended by the manufacturer, contains a CC discharge with 1C. Afterward, a CCCV phase (CC phase with 1C–2.8 V and CV phase until the cut-off current was below C/10) was performed to reach the fully-charged state of the battery. The resting time between charge and discharge was 1 h to allow the battery

to return to an electrochemical equilibrium condition. The described capacity test was repeated at least three times, and the obtained capacity of the last 1C discharge was considered to be the nominal capacity when the difference in capacity between the last two tests was less than 1 %.

Afterward, a quasi-stationary OCV test with C/10 in charge and discharge direction with a 2 h relaxation phase in between was used to obtain the OCV curve and approximate the OCV-SOC relationship of the battery. In addition, the capacity of the quasi-equilibrium state is also obtained in the qOCV test.

Lastly, an HPPC test was performed to measure the ohmic and polarization impedances at different SOC levels, which can be related to battery kinetics performance. HPPC tests were performed at SOC = 80 %, 60 %, 40 %, and 20 % with a C-rate of 4C in charge and discharge direction.

2.3. Electrochemical test

After the cyclic aging test was completed, EIS measurements at different SOCs were performed on a battery cycled at 100 % DOD with a 1.5 V cut-off voltage and 76.5 % remaining useful capacity compared to the nominal capacity, as well as a pristine battery. The impedance of the cells was measured using a Biologic VMP3 potentiostat. The tests were performed in a thermal chamber to maintain a constant ambient temperature of 25 °C. The cell was first charged with C/10 to 2.8 V and then discharged at C/10, while impedance was measured after each 10 % SOC decrease. A rest period of 12 h was undertaken before each impedance measurement. The EIS measurements were performed in galvanostatic mode within a frequency range of 10 kHz to 10 mHz with 10 A oscillation amplitudes. Fifteen points per decade were recorded during the measurement.

Additionally, another battery cycled at 100 % DOD 1.5 V cut-off voltage with 78.4 % remaining useful capacity and a pristine battery was opened in a glove box filled with argon to extract the electrode material. Subsequently, coin cells with anode and cathode material vs. Li/Li^+ were assembled, and the half-cell open circuit potential (OCP) curves were measured using a low current measurement (C/50 in charge and discharge direction).

3. Results and discussion

3.1. Thermodynamic and kinetic loss contributions to capacity fade

The aging of the battery is mainly reflected in the degradation of the electrode material, which can be categorized into thermodynamic degradation and kinetic degradation, depending on the properties. To differentiate the dominant factors contributing to degradation under different cycling conditions, we divided the capacity loss of the battery into losses caused by thermodynamic degradation and losses caused by

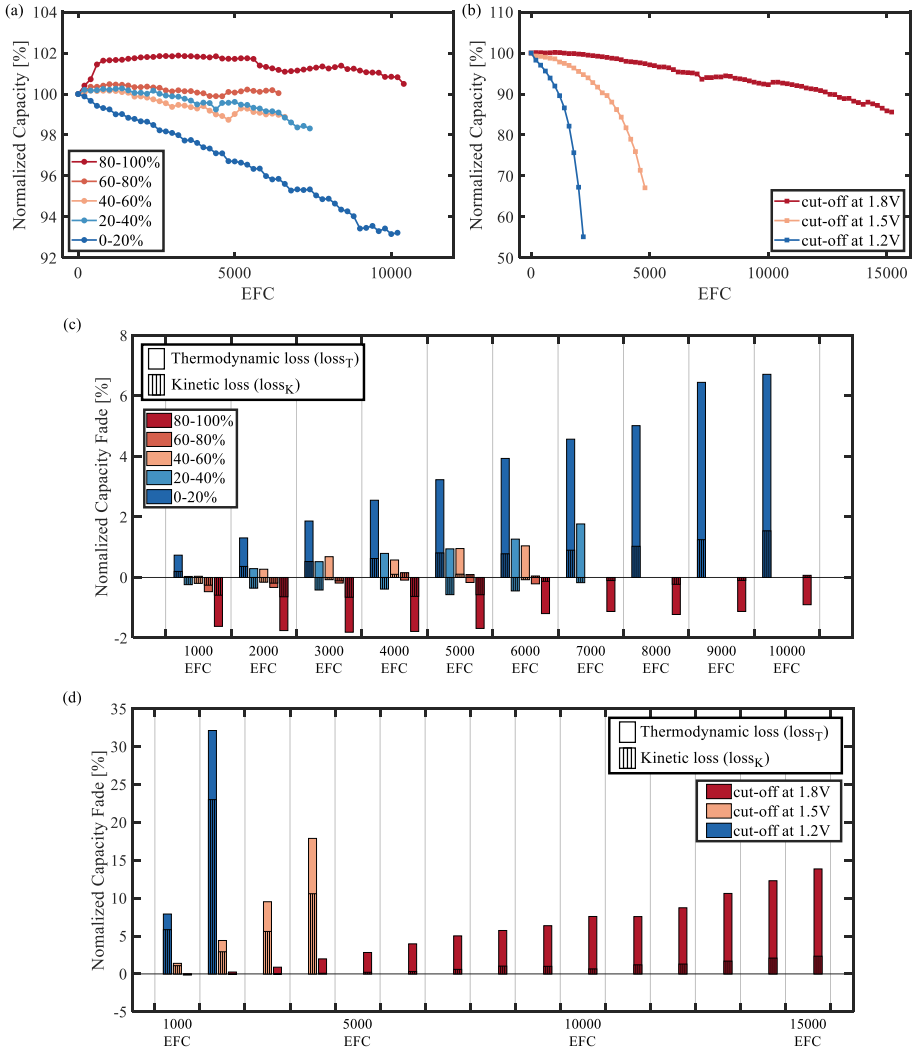

Fig. 4. Results of the cyclic aging: Normalized capacity over equivalent full cycle (EFC) for cells cycled at (a) different SOC intervals and (b) different discharge cut-off voltages. The losses of thermodynamic and kinetic degradation for cells cycled at (c) different SOC intervals and (d) different discharge cut-off voltages.

kinetic degradation. The normalized capacities and their thermodynamic/kinetic losses under different cycling conditions are summarized in Fig. 4. The normalized capacities are normalized based on the nominal capacities at 1 C conditions, which includes the effect of kinetic degradation. In addition, the proportion of thermodynamic and kinetic losses to the total capacity loss is also shown in Table 1. The losses of thermodynamic and kinetic degradation are calculated by Eqs. (1) and (2)

$$loss_T = \frac{Q_1^{Eq} - Q_n^{Eq}}{Q_1^{Eq}} \cdot 100\% \quad (1)$$

$$loss_K = \frac{(Q_n^{Eq} - Q_n^{1C}) - (Q_1^{Eq} - Q_1^{1C})}{Q_1^{Eq}} \cdot 100\% \quad (2)$$

Where $loss_T$ and $loss_K$ are the thermodynamic and kinetic losses, respectively. Q^{Eq} and Q^{1C} are the capacities at near equilibrium conditions and 1 C, respectively, and n represents the number of cycles. Fig. 4 (a) shows the results of the capacity for batteries cycled at different SOC intervals. The cells cycled at 0–20 % showed the strongest capacity fade, while for cells cycled at 80–100 %, the capacity increased within the first 800 cycles. Overall, capacity degradation increases as the SOC decreases by 20 % DOD. This capacity fading behavior is exactly opposite to graphite-based cells, which degrade fastest at high SOC intervals [21].

Fig. 4(b) shows the evolution of the capacity for cells cycled at 100 % DOD with different discharge cut-off voltages. Lower cut-off voltage results in higher capacity fade. Fig. S2 in the Supplementary material shows the discharge capacity of the pristine battery for different cut-off voltages. Compared to the battery capacity extracted with 1.5 V cut-off voltage, the capacity at 1.8 V and 1.2 V cut-off voltage decreased by 0.31 % and increased by 0.24 %, respectively. Although the cut-off voltage showed a minor effect on the initial capacity, the cycle life decreased immensely when a lower cut-off voltage was used. The final remaining normalized capacity of the battery cycled with a 1.8 V cut-off voltage is 85.6 %. Therefore, for comparison purposes, 85.6 % is defined as the end-of-life of the battery. The batteries with 1.2, 1.5, and 1.8 V cut-off voltages reach the end-of-life after 1292, 3376, and 15,200 EFCs.

The trends of the thermodynamic and kinetic degradation losses as a function of EFC are shown in Fig. 4(c) and (d). The solid-colored squares represent the thermodynamic losses, while the shaded squares depict the kinetic losses. The sum of these two components represents the total capacity loss. It should be noted that the thermodynamic loss can be negative in some states, indicating that the capacity under near-equilibrium conditions after cycling is actually greater than that before cycling ($Q_n^{Eq} > Q_1^{Eq}$). Additionally, the negative kinetic losses suggest that the capacity reduction due to the current after cycling is less than that before cycling $\left(Q_n^{Eq} - Q_n^{1C}\right) < \left(Q_1^{Eq} - Q_1^{1C}\right)$. However, the presence of negative capacity losses can complicate the accurate determination of the percentage contributions of the thermodynamic and kinetic degradation to the total capacity loss. Therefore, for the analysis presented in Table 1, only the results from the cells cycled in the 0–20 % SOC interval and the cells cycled at different discharge cut-off voltages were selected. Specifically, the cell in the 0–20 % SOC interval was analyzed at the end of all cycles (10200th EFC), while the cells with different cut-off voltages were at the end-of-life.

Table 1
Proportion of thermodynamic and kinetic losses to total capacity loss.

Cycle condition	Thermodynamic loss	Kinetic loss	Total loss	Nominal capacity
0–20 %	1.36 Ah /76.6 %	0.42 Ah /23.4 %	1.78 Ah (6.8 %)	24.53 Ah (93.2 %)
0–100 % (1.8 V)	3.03 Ah /83.3 %	0.61 Ah /16.7 %	3.64 Ah (14.4 %)	21.68 Ah (85.6 %)
0–100 % (1.5 V)	1.51 Ah /41.2 %	2.14 Ah /58.8 %	3.65 Ah (13.8 %)	22.80 Ah (86.2 %)
0–100 % (1.2 V)	0.94 Ah /26.6 %	2.57 Ah /73.4 %	3.51 Ah (13.4 %)	22.68 Ah (86.6 %)

For the batteries cycled at different SOC intervals, as shown in Fig. 4 (c), the thermodynamic loss accounts for a larger proportion of the total capacity fade compared to the kinetic loss. Specifically, the thermodynamic loss is most prominent in the 0–20 % SOC interval, being greater than in any of the other SOC intervals (20–40 %, 40–60 %, 60–80 %, 80–100 %). Furthermore, the cells cycled in the 0–20 % SOC interval exhibited an increase in the kinetic loss with the number of cycles, although the percentage contribution of the kinetic loss did not change significantly over cycling in this SOC interval.

As shown in Fig. 4(d) and Table 1, the batteries cycled at different discharge cut-off voltages exhibited distinct degradation behaviors. For the battery cycled at 1.8 V cut-off voltage, the thermodynamic degradation dominates. In contrast, for the cells cycled at 1.2 V and 1.5 V cut-off voltages, the kinetic degradation becomes the primary factor contributing to capacity fade. Moreover, the percentage of kinetic degradation increases as the cut-off voltage decreases. This suggests that the rapid capacity degradation observed at lower cut-off voltages may be due to accelerated kinetic degradation processes. This finding may also help explain why the cells cycling in the 0–20 % SOC interval degrade more rapidly than cells cycling in other SOC intervals, as the accelerated kinetic degradation appears to be a key factor in the more severe degradation at lower voltage.

3.2. Thermodynamic degradation

The thermodynamic degradation of the battery is mainly indicated by the reduction of maximum capacity and the change of voltage curve under near equilibrium conditions. Two commonly used methods to analyze the changes in the OCV curve are incremental capacity analysis (ICA) and differential voltage analysis (DVA). Both methods compare the rate of capacity change to the rate of voltage change, which can be used to analyze the phase change process of the battery. The key difference is that ICA shows the phase transition process against voltage, while DVA shows the phase transition process against capacity. To better distinguish the contribution of different thermodynamic degradation to capacity fade, the DVA approach is particularly useful. It can identify the capacity loss associated with different phase change processes. Additionally, the OCV reconstruction analysis proposed in the literature has also been used to separate the effects of the two electrodes and explain the different degradation modes under various aging conditions [13,33]. To determine the contributions of different aging modes to the thermodynamic losses, the effects of these aging modes can be decoupled by combining the DVA and OCV reconstruction analyses. This allows for an analysis of the relationship between capacity degradation and the different aging modes in the various regions from the DVA.

3.2.1. Differential voltage analysis under different cycle conditions

The DVA for cells cycled at different SOC intervals and cut-off voltages are shown in Figs. 5 and 6, respectively. In order to clearly distinguish the contribution of different degradation modes to capacity degradation, it has been suggested in the literature that the DVA curve can be analyzed by dividing it into regions [15]. Fig. 5(a) shows an example of the DVA curve after 2000 EFCs of the battery cycled at 80–100 % SOC. The DVA curve is divided into three plateau regions, which are separated by dashed lines and labeled as P1-3. The corresponding capacities of the divided platform regions are marked as Q_A, Q_B, and Q_C. The capacity changes of Q_A and Q_C are jointly attributed to LAM_{cat}, LAM_{an}, and LLI, while Q_B is only related to LAM_{cat} [15,34]. In addition, the P3 region can only be identified after aging, which will be discussed later.

Fig. 5 shows the DVA curves of the batteries under all investigated cyclic aging conditions. As mentioned, the anode has a constant voltage plateau in the two-phase transformation region, so the phase transition process of the P2 and P3 regions comes from the lithium-cobaltate-oxide

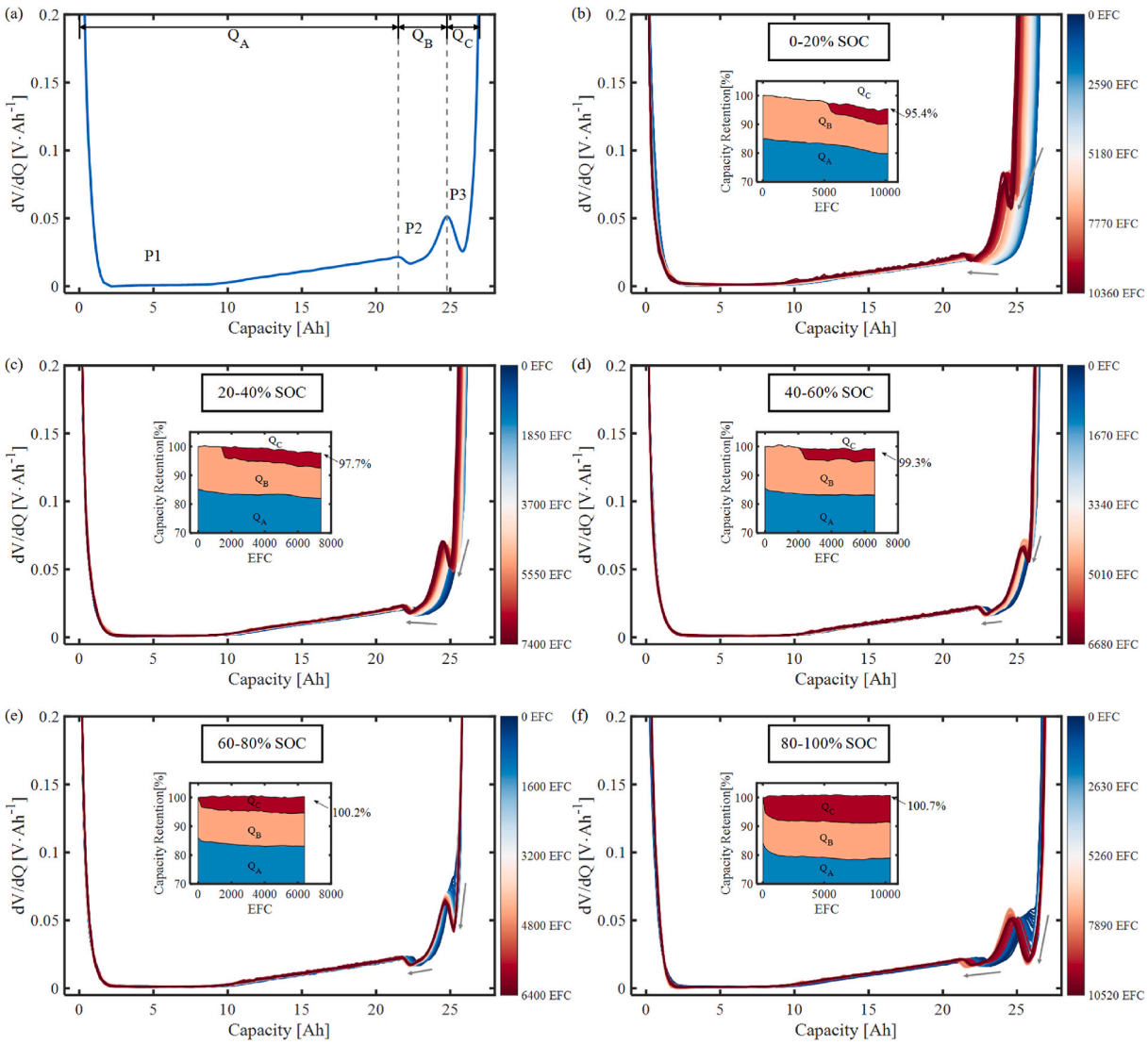

Fig. 5. (a) Example of the relationship between Q_A, Q_B, Q_C and P1, P2, P3 in the DVA curve. DVA curves obtained from the OCV test upon cycling at (b) 0%–20 %, (c) 20%–40 %, (d) 40%–60 %, (e) 60%–80 %, (f) 80%–100 %.

(LCO) cathode material. The subplots also show the changes in Q_A, Q_B and Q_C over aging, which are identified from the DVA curves of the respective cycle numbers. For a pristine battery, the Q_C capacity corresponding to the P3 region is not within the lithiation range of the full cell. However, after a certain amount of aging, the P3 region gradually increases, such that Q_C becomes identifiable. For batteries cycled at 0–20 %, Q_C can be identified after 5000 EFCs. For batteries cycled at 20–40 % and 40–60 %, Q_C can be identified at around 2000 EFCs. The Q_C can be identified after the first few cycles for batteries cycled at 60–80 % and 80–100 %. The phase transition process corresponding to the P3 region only occurs in the high voltage region of the cathode, and the Q_C identified indicates that the voltage of the cathode becomes higher when the charge cut-off is reached and the cathode is in a lower lithiation state. The reason for Q_C being identified earlier when cycling in the high SOC intervals may be that the high voltage region of the cathode will be reached earlier at this time, which could be caused by either a faster decay of the cathode material or a slower decay of the anode material.

Fig. 6 shows the DVA curve evolution over aging for the cells cycled between 0–100 % SOC with different cut-off voltages. The shape of the DVA curve for the batteries cycled at 1.2 V and 1.5 V cut-off voltages changes significantly after aging, which is quite different from that of the batteries cycled with 20 % DOD, as shown in Fig. 5. However, the DVA curves exhibit the same aging trend for batteries with a 1.8 V cut-off voltage. During the aging process, Q_A decreases the most, while Q_C increases with decreasing cut-off voltage. Especially for the battery cycled at 1.2 V cut-off condition, Q_C increases rapidly after the accelerated degradation in Q_A and eventually makes up nearly half of the overall battery capacity at the cycle end. As mentioned before, Li_xCoO_2 materials are designed to work in the range of $x > 0.5$ to ensure a long cycle life. However, the increased capacity of Q_C comes from the capacity of Li_xCoO_2 material where $x < 0.5$, which indicates that the cathode suffers from severe degradation. For the cell with a 1.8 V cut-off voltage, the reduction of both Q_B and Q_C is not significant, while the decrease in Q_A is the main reason for the reduction of the full cell capacity. For the battery with a 1.8 V cut-off voltage, the decrease of both Q_B and Q_C is slow, while the decrease of Q_A is the main reason for the reduction of the overall battery capacity.

The DVA curves based on the OCV curves show different thermodynamic degradations under different cycling conditions. For cycling conditions with different SOC intervals, lower SOC intervals lead to higher capacity fade, while higher SOC intervals lead to higher shape change of the DVA curve. For cycling conditions with different cut-off voltages, lower cut-off voltages lead to higher capacity fade and

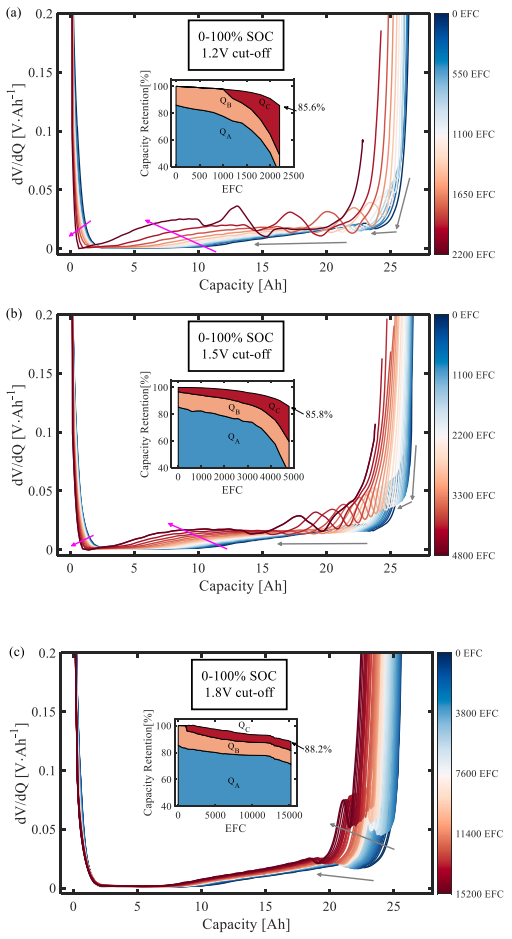

Fig. 6. DVA curves obtained from the OCV test upon cycling at (a) 1.2 V cut-off, (b) 1.5 V cut-off, and (c) 1.8 V cut-off.

bigger shape change of the DVA curve.

3.2.2. *OCV reconstruction analysis under different cycle conditions*

As presented in various literature, the method of OCV reconstruction can simulate various scenarios of battery degradation via a synthetic method based on specific electrode behavior by properly adjusting the N/P ratio (Q_{NE}/Q_{PE}) and the extent of degradation between two electrodes [13,33]. This study employed a particle swarm algorithm to adjust both electrodes to minimize the error between the difference in cathode OCP minus anode OCP and the full cell OCV. Subsequently, by comparing the relationship between electrode OCP and full-cell OCV before and after aging, the degradation modes can be categorized into LAM_{cat}, LAM_{an}, and LLI. The N/P ratio for the full cell at the begin of life (BOL) is 0.75, and the electrode balancing under different separate degradation modes is shown in Fig. 7. The detailed OCV reconstruction method and the definition of the degradation modes are provided in Note S3, Supplementary material.

Fig. 7(a and b) show the evolution of the electrode balancing and DVA curve along with battery aging under LLI. When LLI occurs, the OCV and DVA curves of the cathode remain consistent, while the anode curve shifts to the right side, leaving the capacity in the low voltage region of the cathode inaccessible. When the LLI is small, both the cathode and anode will enter a lower lithiation state at the charge cut-off voltage, increasing the voltage of the cathode and anode. As a result, the increased unused capacity of the cathode in the lower voltage region will be supplemented by the capacity obtained from the cathode in the higher voltage. At this time, the LLI has little effect on the battery capacity.

When the LLI exceeds a certain threshold, the anode voltage at the charge cut-off will reach the plateau region, where the anode voltage does not increase much with the deintercalation of lithium in the anode. Therefore, the cathode voltage is limited by the full cell voltage and will not increase either, which means the increased unused capacity of the cathode in the low voltage region cannot be supplemented by increasing the cut-off voltage. And the LLI will lead to rapid degradation of battery capacity.

Fig. 7(b) shows that LLI leads to a decrease in capacity corresponding to the P1 region, while before LLI reaches the threshold, the increased cathode voltage allows more capacity corresponding to the P3 region, which partly supplements the capacity loss in the P1 region and slows down the capacity fade of the battery. When the LLI exceeds the threshold, the capacity corresponding to the P3 region will no longer increase, and the LLI will directly lead to battery capacity degradation.

Fig. 7(c and d) show the evolution of the OCV curve and DVA curve along with battery aging under LAM_{cat}. When LAM_{cat} occurs, the OCV and DVA curves of the anode remain constant, and the cathode curves shrink by a certain proportion while keeping their right end fixed. The subplot in Fig. 7(c) shows that the charge cut-off points of the full cell change by only 0.8 % (0.2Ah) when LAM_{cat} reaches 15 %. Therefore, the full cell capacity degradation is dominated by the change in the discharge cut-off. When the LAM_{cat} is small, e.g., less than 2.5 %, the discharge cut-off is still due to the rapid voltage rise of the anode. At this time, LAM_{cat} will not lead to battery capacity degradation. However, when the LAM_{cat} exceeds a certain threshold, the discharge cut-off will be reached due to the rapid voltage drop of the cathode, and the cathode will be the limiting factor for battery capacity. Fig. 7(d) shows that the capacity corresponding to P1 and P2 regions decreases as LAM_{cat} increases. When LAM_{cat} exceeds 5 %, the cathode curve almost overlaps with the full cell curve on the left side of Fig. 7(d). At this time, LAM_{cat} will lead to an equal amount of degradation in the battery capacity.

Fig. 7(e and f) show the evolution of the OCV curve and DVA curve along with battery aging under LAM_{an}. When LAM_{an} occurs, for the full cell, the left side of its OCV curve almost overlaps with the pristine cell, and the right side shrinks along with the LAM_{an}. Fig. 7(f) shows that when only LAM_{an} occurs, the anode and the full cell DVA curves are almost overlapped at both charge cut-off and discharge cut-off. As for the full battery, the LAM_{an} will directly lead to the loss of full cell capacity. At this time, the full cell capacity is limited by the anode capacity. And LAM_{an} will lead to the same amount of degradation in the battery capacity.

As mentioned above, the method of OCV reconstruction can quantitatively analyze the degradation modes occurring during cyclic aging. The evolution of the trajectories for the three degradation modes under different SOC intervals is summarized in Fig. 8. The LAM_{cat} for the batteries cycled at 0–20 % SOC exhibits a nearly linear increasing decay rate in Fig. 8(a). On the contrary, for all other operating points with higher SOC intervals, the cathode material will enter a stable aging stage with a low degradation rate at about 2000 EFCs. At lower SOCs, the first-order phase transition between the insulating $Li_{0.94}CoO_2$ phase and the metallic $Li_{0.75}CoO_2$ phase causes a larger volume change, possibly fragmenting the material and reducing the cathode capacity [35,36]. While at higher SOCs, the volume change of the material is smaller. For batteries cycled between 80–100 % SOC, the cathode material degrades rapidly in the first 1000 cycles. This may be due to the lattice distortion and inter-slab lithium/vacancy ordering caused by the transformation between the metallic and monoclinic phases [37]. After 1000 cycles, the formation of the cathode electrolyte interphase (CEI) protects the cathode material from further degradation [38,39].

Fig. 8(b) shows the evolution of LAM_{an} during cyclic aging. LAM_{an} decreases with increased SOC and even decreases to below zero when cycled above 60 % SOC. The capacity of the anode increases in the high SOC interval, probably due to the gassing behavior that increases the pressure within the LTO material and causes cracking. This cracking

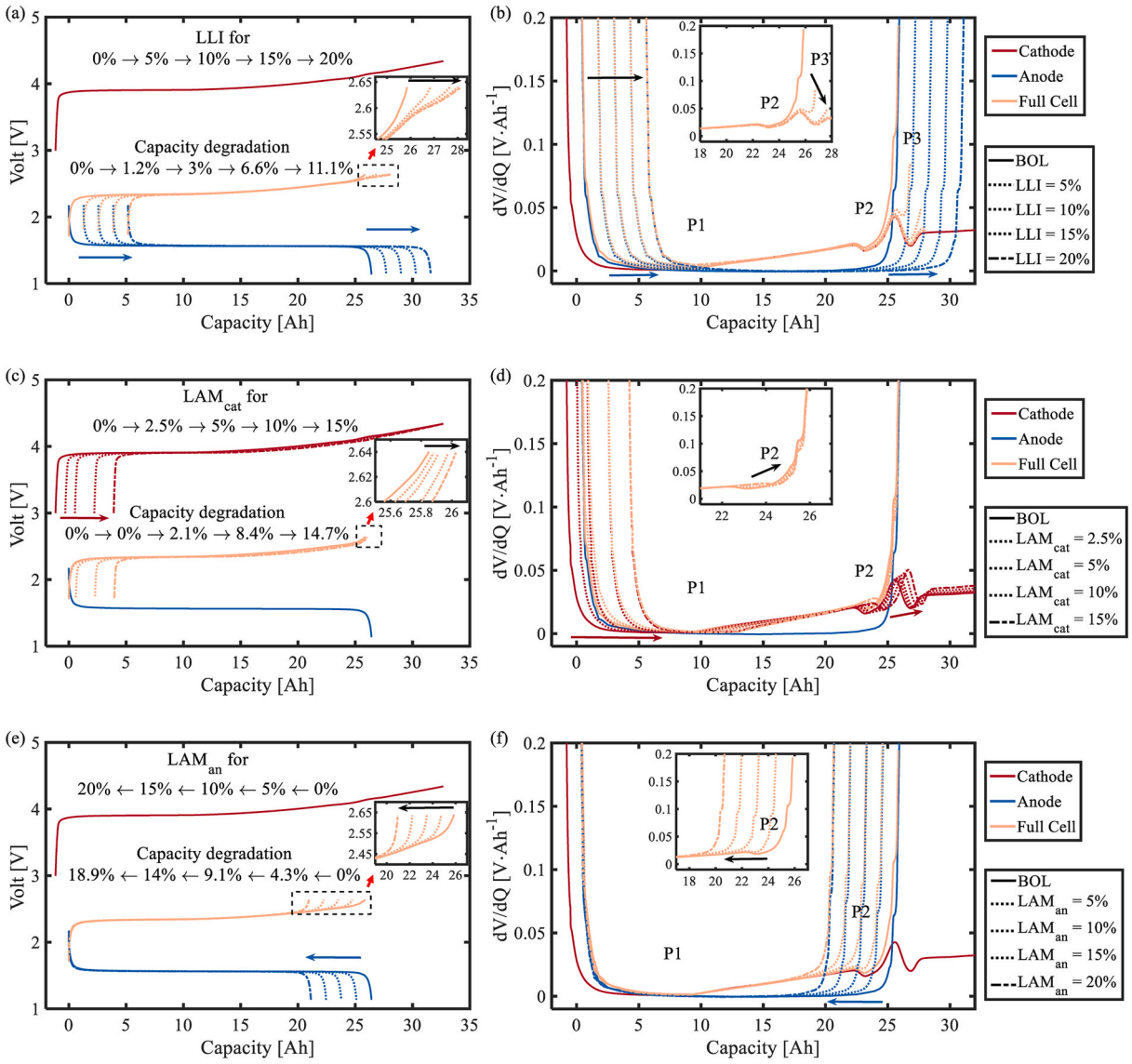

Fig. 7. Evolution of electrode balancing under (a) LLI, (c) LAM_{cat}, (e) LAM_{an}. Evolution of DVA curve under (b) LLI, (d) LAM_{cat}, (f) LAM_{an}.

may approximate the phenomenon of electrochemical milling, which would increase the active area of the LTO material [11,40]. On the contrary, the anode capacity decreases more significantly at lower SOC intervals. However, the reason for this behavior is not clear. In the literature, the solid electrolyte interphase (SEI) was generated at high SOC, which may protect anode materials from degradation [41,42]. However, the results in Section 3.2 show that no SEI was detected. Further investigations will attempt to analyze the side reactions of LTO material at lower SOC intervals and thus find the cause of the aging behavior.

Fig. 8(c) shows the LLI evolution for each operating point. Except for the batteries cycled at 0–20 % SOC, the LLI of all other batteries is increased at a reduced rate, which is similar to the LAM_{cat}. Here, several factors could play an important role. First, for batteries cycled at 80–100 % SOC, LAM_{cat} might accumulate to a thicker CEI during cycling, consuming lithium ions during cycling [38,39]. Second, for batteries cycled at SOCs below 80 %, the SOC dependence of LLI mainly correlates to the passive electrode effect [11,43]. Considering that the SOC of the battery was approximately 80 % before cycling and the anode geometry of this battery is larger than the cathode (shown in Note S4, Supplementary material), an anode overhang would cause additional LLI during cycling at SOCs above 80 % while cycling below 80 % should increase the lithium inventory. Hence, this can describe the increasing LLI at cycling SOC between 80–100 % and the proportionally lower amount of LLI for cells cycled between 40–60 % SOC and 60–80 % SOC. However, the batteries cycled in the lower SOC intervals of 0–20 % and 20–40 % show different characteristics, which may be caused by the other side reactions during the two-phase transition region of the Li_xCoO_2 at $0.75 \leq x \leq 0.93$.

Fig. 8(d) illustrates the evolution of the N/P ratio during cyclic aging. For the batteries cycled in the intermediate SOC interval, the N/P ratio is always below 0.8 after aging. In contrast, for the batteries cycled in the 80–100 % SOC interval, the N/P ratio rises rapidly in the first 1000 cycles. This is due to the combined effect of a rapid decrease in the capacity of the cathode and a recovery of the capacity of the anode. The N/P ratio reaches around 0.82 before gradually entering a stage of more stable change. Interestingly, despite the different initial capacities and aging rates, the batteries cycled in the 80–100 % SOC interval and the 0–20 % SOC interval exhibit a convergence of their N/P ratios after 7000 cycles. This suggests that the ratio of the positive and negative capacity decline rates in these two SOC intervals becomes the same at this later stage of cycling.

Additionally, OCV reconstruction analysis was performed on batteries cycled with 100 % DOD at different cut-off voltages. As shown in

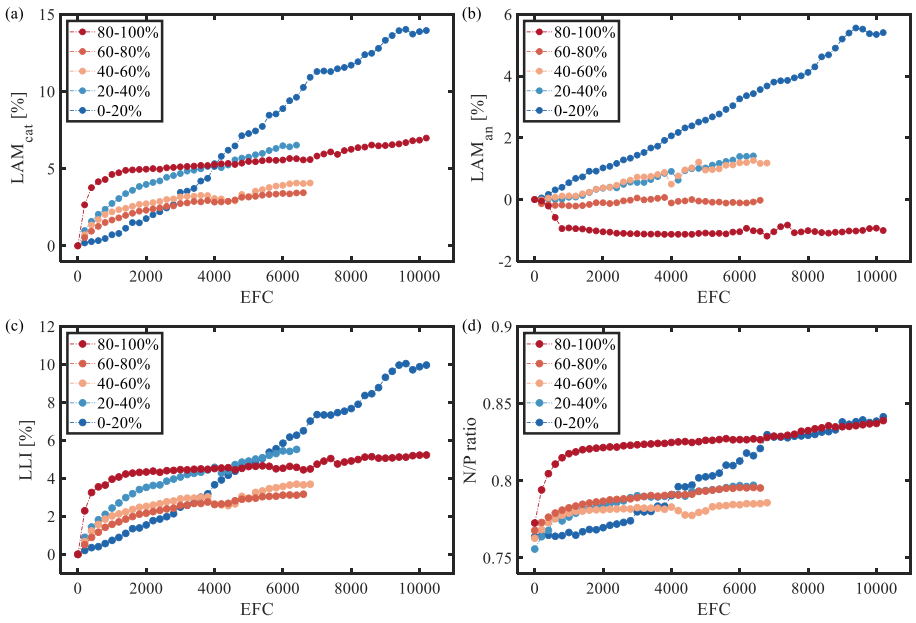

Fig. 8. The trajectories of battery degradation modes over cycle number at different SOC intervals: (a) LAM_{cat}, (b) LAM_{an}, (c) LLI, and (d) N/P ratio.

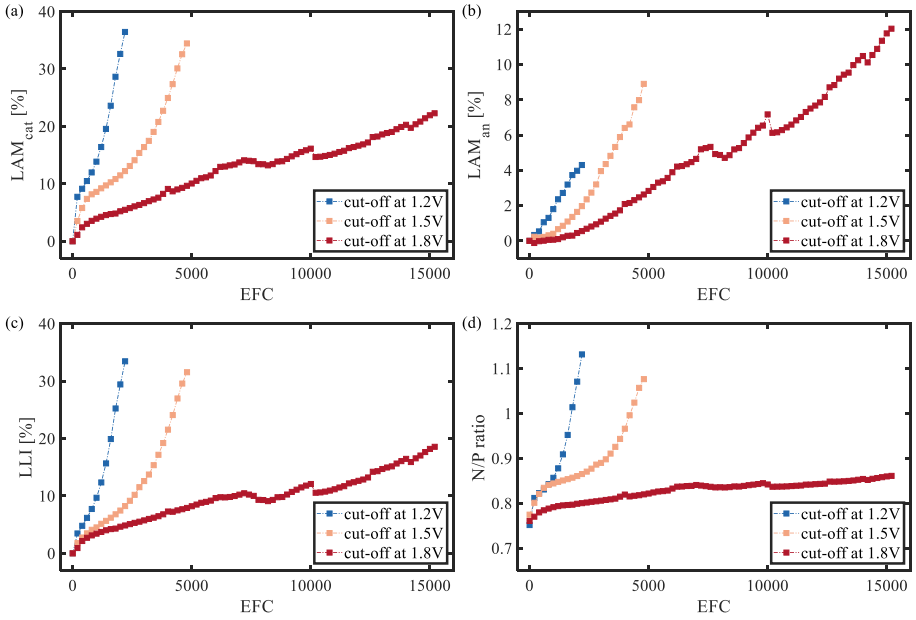

Fig. 9. The trajectories of battery degradation modes over cycle number under different discharge cut-off voltages: (a) LAM_{cat}, (b) LAM_{an}, (c) LLI, and (d) N/P ratio.

Fig. 9, lowering the discharge cut-off voltage will accelerate the battery's aging process and all degradation modes. By comparing Fig. 9(a and b), we can see that by lowering the cut-off voltage from 1.8 V to below 1.5 V, LAM_{cat} increases from 20 % to more than 30 %, while LAM_{an} decreases from 10 % to less than 7 %. This shows that reducing the cut-off voltage has a stronger impact on the degradation of cathode material than on anode material. Moreover, when the LAM_{cat} is dominating, the cathode will become the main limitation of the battery discharge cut-off as shown in Fig. 7(c). Lower cut-off voltages will lead the cathode to an over-lithiated state or even convert to Li_2O and Co metal, which will cause irreversible damage to the cathode material and further accelerate battery degradation [44].

Compared to batteries cycled at 20 % DOD, the batteries cycled at 100 % DOD (1.5 V cut-off) suffered severe degradation after fewer EFCs. This demonstrates that higher cycle depths lead to higher stresses, which may contain multiple aging mechanisms. Cathode materials will undergo more phase changes when working in a larger working range, resulting in a larger volume change and more severe material fragmentation. In addition, the CEI formed at high SOC will dissolve at low SOC, which fails to generate a stable passivation layer to protect the cathode material and consumes many lithium ions, leading to LLI. For anode materials, higher stresses will trigger more severe gas behavior, which will consume electrolytes and lead to kinetic degradation of the battery.

The N/P ratio behavior in Fig. 9(d) also reveals distinct differences between the 100 % DOD and 20 % DOD cycling conditions. For the battery cycled with a 1.8 V cut-off voltage, the final N/P ratio is similar to the batteries cycled in the 80–100 % and 0–20 % SOC intervals, remaining around 0.85. In contrast, the N/P ratios for the batteries cycled with 1.5 V and 1.2 V cut-off voltages continued to rise due to

severe LAM_{cat}. In these cases, the N/P ratio eventually exceeded 1.0, indicating that the positive electrode capacity had become less than the negative electrode capacity. This divergent N/P ratio behavior highlights the significant impact of the discharge cut-off voltage. The higher 1.8 V cut-off was able to maintain a balanced N/P ratio of around 0.85, even under the more demanding 100 % DOD cycling. However, the lower 1.5 V and 1.2 V cut-offs accelerated the degradation of the positive electrode to the point where it became the limiting factor, causing the N/P ratio to exceed 1.0.

Another observation is that cells cycled at a lower cut-off voltage showed accelerated capacity fade. To investigate this phenomenon, the identified cathode and anode capacities are compared to the full cell capacity in Fig. 10 for cells cycled at cut-off voltages less than 1.5 V. The cathode has experienced severe degradation, and its capacity is even less than that of the anode after aging, as shown in Fig. 10(a and b). In the initial stage of aging, the full-cell capacity shows the same trend as the anode capacity, indicating that the anode limits the full-cell capacity at this time. With the aging process, the cathode gradually becomes the limiting factor for the full cell capacity due to its rapid capacity fade. At this time, the full cell exhibits a similar degradation trend with the cathode, which is faster than at the initial state. However, the cathode capacity fades much more slowly for batteries cycled at the cut-off voltage of 1.8 V, as shown in Fig. 10(c). Under this condition, the cathode capacity is always larger than the anode capacity. Furthermore, the full battery capacity is limited by the anode and does not show accelerated capacity fade.

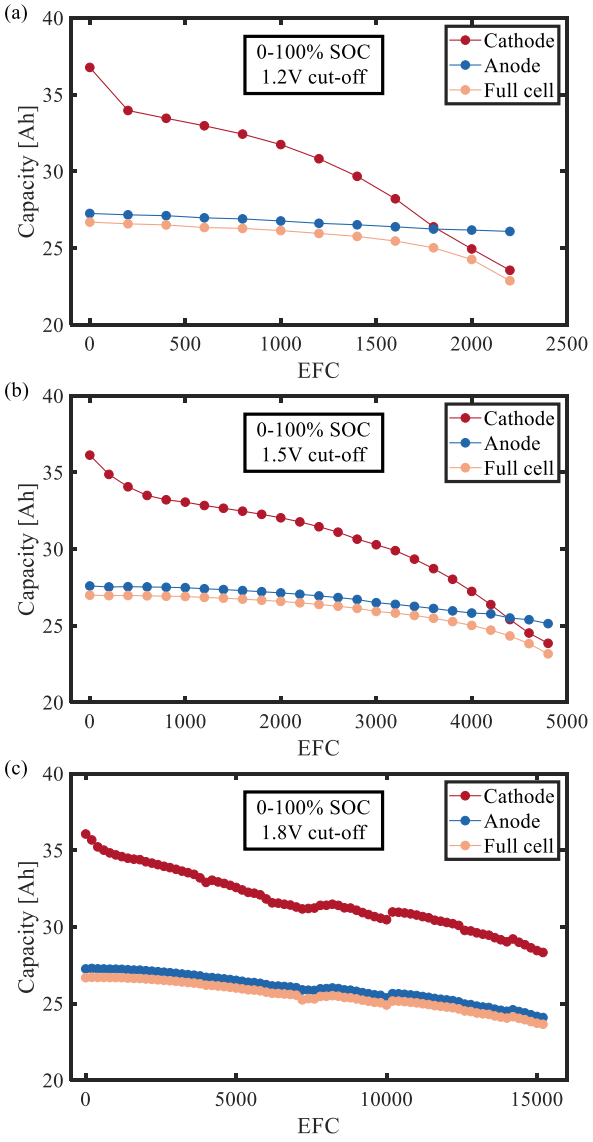

Fig. 10. Evolution of cathode and anode capacity and full cell capacity upon cycling at (a) 1.2 V cut-off, (b) 1.5 V cut-off, and (c) 1.8 V cut-off.

Batteries cycled at lower SOC intervals showed pronounced LLI, LAM_{cat}, and LAM_{an} compared to higher SOC intervals. However, cells cycled between 80–100 % SOC were subject to an initial significant amount of LLI and LAM_{cat} before reaching a stable state, which could be attributed to the passive electrode effect and the formation of a CEI. Additionally, the anode capacity showed a capacity increase, leading to an initial capacity increase in the full cell. The analyzed degradation mechanisms under all other operating conditions between 20–80 % SOC showed a converging behavior, while all degradation modes increased with decreasing SOCs. This opposite phenomenon compared to graphite cells could be mainly due to the different aging properties of the electrode materials. For graphite cells, the fast degradation is mainly due to the structural damage caused by the intense volume change of graphite anode at high SOC [9,46]. However, in LTO cells, the anode LTO material degrades much slower compared to the cathode. Therefore, the cathode material, which degrades faster at low SOC, dominates the degradation of LTO cells.

Cycling at 100 % DOD with different cut-off voltages revealed that lowering the discharge cut-off voltage accelerated the degradation across all aging modes, leading to faster battery aging. This is an important finding, as LTO batteries typically have an N/P ratio of less than 1.0. This allows the degradation of the cathode material during early aging to have a reduced impact on the overall battery capacity. However, the data shows that at lower discharge cut-off voltages, the degradation of the positive electrode material becomes more severe compared to the negative electrode. As a result, the final N/P ratio ends up greater than 1.0. Although the capacities at the different cut-off voltages differ by only 0.3 % (0.07 Ah), the impact on cycle life is substantial. Lowering the discharge cut-off voltage to 1.2 V reduced the cycle life by more than half while increasing the cut-off to 1.8 V more than tripled the cycle life.

3.2.3. *Contribution of different aging modes to thermodynamic losses*

According to the results of the analysis in the previous section, different aging modes can impact battery capacity in four main ways:

1) LLI causes the full cell capacity to fade due to the early anode cut-off during discharge.
2) LLI extends the voltage range of the cathode at the charging cut-off, leading to an increase in battery capacity.
3) LAM_{cat} decreases the full cell capacity due to the early cathode cut-off during discharge.
4) LAM_{an} decreases the full cell capacity due to the early anode cut-off during charging.

However, the contribution of multiple aging modes to the thermodynamic losses in the full cell capacity fade cannot be obtained by simple superposition. Instead, it needs to be analyzed according to the different phase transition regions. Together with the results of DVA and OCV reconstruction analyses, the following insights were obtained:

- Q_A corresponding to the P1 region is affected by both LAM_{cat} and LLI.
- Q_B corresponding to the P2 region is affected by LAM_{cat} only.
- Q_C corresponding to the P3 region is affected by both LAM_{an} and LLI.

Eq. (3) describes the effect of different aging modes on the regional capacity contributions.

$$\begin{cases} \Delta Q_A = \Delta Q_A^{LAM_{cat}} + \Delta Q_A^{LLI} \\ \Delta Q_B = \Delta Q_B^{LAM_{cat}} \\ \Delta Q_C = \Delta Q_C^{LAM_{an}} + \Delta Q_C^{LLI} \end{cases} \tag{3}$$

ΔQ_A, ΔQ_B and ΔQ_C are the capacity loss in Q_A, Q_B, and Q_C, respectively, due to the thermodynamic degradation. Within the capacity loss ΔQ_A, $\Delta Q_A^{LAM_{cat}}$ represents the loss due to the LAM_{cat}, and ΔQ_A^{LLI} represents the loss due to the LLI. In contrast, Q_B is only affected by the LAM_{cat} and can be obtained directly from the DVA. To decouple the individual effects of the two aging modes in Q_A and Q_C, the capacity loss was simulated for each aging mode separately as well as their combined effect, as shown in Fig. 11.

The impact of LAM_{cat} and LLI on Q_A is shown in Fig. 11(a). When only LAM_{cat} occurs, the cathode OCP curve shrinks to the right (red solid line). Combining this aged cathode curve with the pristine anode curve yields the full-cell curve under the influence of LAM_{cat} only (red dashed line). This allows us to calculate the loss in Q_A due to LAM_{cat} only, denoted as $\Delta Q_{A,only}^{LAM_{cat}}$. Similarly, the anode OCP curve shrinks to the right (blue solid line) when only LLI occurs. Combining this shifted anode curve with the pristine cathode curve yields the full-cell curve under the influence of LLI only (blue dashed line). And calculate the loss in Q_A due to LLI only, denoted as $\Delta Q_{A,only}^{LLI}$. However, the total loss in Q_A under the combined effect of LAM_{cat} and LLI, denoted as $\Delta Q_A^{LAM_{cat}+LLI}$, is not directly related to either $\Delta Q_{A,only}^{LAM_{cat}}$ or $\Delta Q_{A,only}^{LLI}$. Therefore, in this paper, Eqs. (4) and (5) are used to approximate the individual contributions of LAM_{cat} and LLI to the total capacity loss in Q_A.

$$\Delta Q_A^{LAM_{cat}} = \Delta Q_A \cdot \frac{\Delta Q_{A,only}^{LAM_{cat}}}{\Delta Q_{A,only}^{LLI} + \Delta Q_{A,only}^{LAM_{cat}}} \tag{4}$$

$$\Delta Q_A^{LLI} = \Delta Q_A \cdot \frac{\Delta Q_{A,only}^{LLI}}{\Delta Q_{A,only}^{LLI} + \Delta Q_{A,only}^{LAM_{cat}}} \tag{5}$$

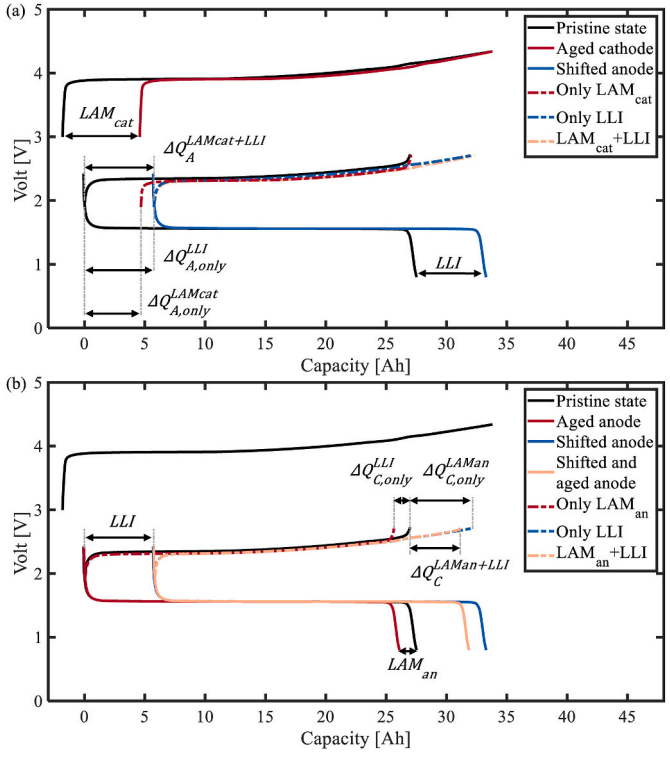

Fig. 11. (a) The effects of LAM_{cat} and LLI in Q_A, and (b) the effects of LAM_{an} and LLI in Q_C.

The impact of LAM_{an} and LLI on Q_C is shown in Fig. 11(b). Similarly, the losses when LAM_{an} or LLI alone occur are denoted as $\Delta Q_{C,only}^{LAM_{an}}$ and $\Delta Q_{C,only}^{LLI}$, respectively. It is worth noting that the anode OCP curve (blue solid line) is shifted to the right due to LLI, which delays the anode cut-off at the end of charging. This allows more material at the cathode to participate in the cell reaction and increases the full cell capacity. This is consistent with the results verified on graphite cells in the literature, and the LTO anode makes this phenomenon more pronounced due to the extremely flat voltage plateau [45]. The contributions of LAM_{an} and LLI in Q_C are calculated by using Eqs. (6) and (7).

$$\Delta Q_C^{LAM_{an}} = \Delta Q_C \cdot \frac{\Delta Q_{C,only}^{LAM_{an}}}{\Delta Q_{C,only}^{LLI} + \Delta Q_{C,only}^{LAM_{an}}} \tag{6}$$

$$\Delta Q_C^{LLI} = \Delta Q_C \cdot \frac{\Delta Q_{C,only}^{LLI}}{\Delta Q_{C,only}^{LLI} + \Delta Q_{C,only}^{LAM_{an}}} \tag{7}$$

The individual contributions of the different aging modes to the overall thermodynamic capacity losses can be obtained by superimposing the capacity losses caused by each aging mode when simulated separately:

$$\begin{cases} Q_{loss}^{LAM_{cat}} = \Delta Q_A^{LAM_{cat}} + \Delta Q_B^{LAM_{cat}} \\ Q_{loss}^{LAM_{an}} = \Delta Q_C^{LAM_{an}} \\ Q_{loss}^{LLI} = \Delta Q_A^{LLI} + \Delta Q_C^{LLI} \end{cases} \tag{8}$$

The contributions of the different aging modes to the total thermodynamic losses of the cells at their respective end-of-life, which are the same as the states in Table 1, are shown in Table 2. The percentage of LAM_{cat} and LAM_{an} is calculated without considering the capacity recovery due to LLI. The result shows that the LAM_{cat} accounts for a significant portion of the total thermodynamic capacity losses. Furthermore, the percentage of capacity loss attributed to LAM_{cat} increases as the cell's cut-off voltage decreases. This trend may be due to the faster degradation of the cathode material at lower cut-off voltages, leading to a more rapid progression of the LAM_{cat} compared to the LAM_{an}. Additionally, for the cells with LTO anodes, the recovery effect of the LLI is highly significant. In fact, LLI does not lead to a decrease in the full cell capacity, but rather results in an increase in capacity under all the cycle conditions.

3.3. Kinetic degradation

The kinetic degradation of the battery is mainly indicated by the increase of the polarization resistance, which is compared for different degradation conditions, as shown in Fig. 12. EIS and DRT have also been used to analyze the mechanism of kinetic degradation in typical cells. However, the DRT problem is inherently ill-posed, which means that the solution may not be unique or may be very unstable [47]. To double-check the results of the DRT analysis, an equivalent circuit (EC) was subsequently developed to model the battery impedance.

Table 2
Contribution of different aging modes to thermodynamic losses.

Cycle condition	Loss by LAM_{cat}	Loss by LAM_{an}	Loss by LLI	Thermodynamic total loss
0–20 %	2.12 Ah /63.3 %	1.22 Ah /36.7 %	−1.98 Ah	1.36 Ah
0–100 % (1.8 V)	3.04 Ah /53.1 %	2.68 Ah /46.9 %	−2.69 Ah	3.03 Ah
0–100 % (1.5 V)	1.38 Ah /66.7 %	0.69 Ah /33.3 %	−0.56 Ah	1.51 Ah
0–100 % (1.2 V)	1.53 Ah /81.2 %	0.35 Ah /18.8 %	−0.94 Ah	0.94 Ah

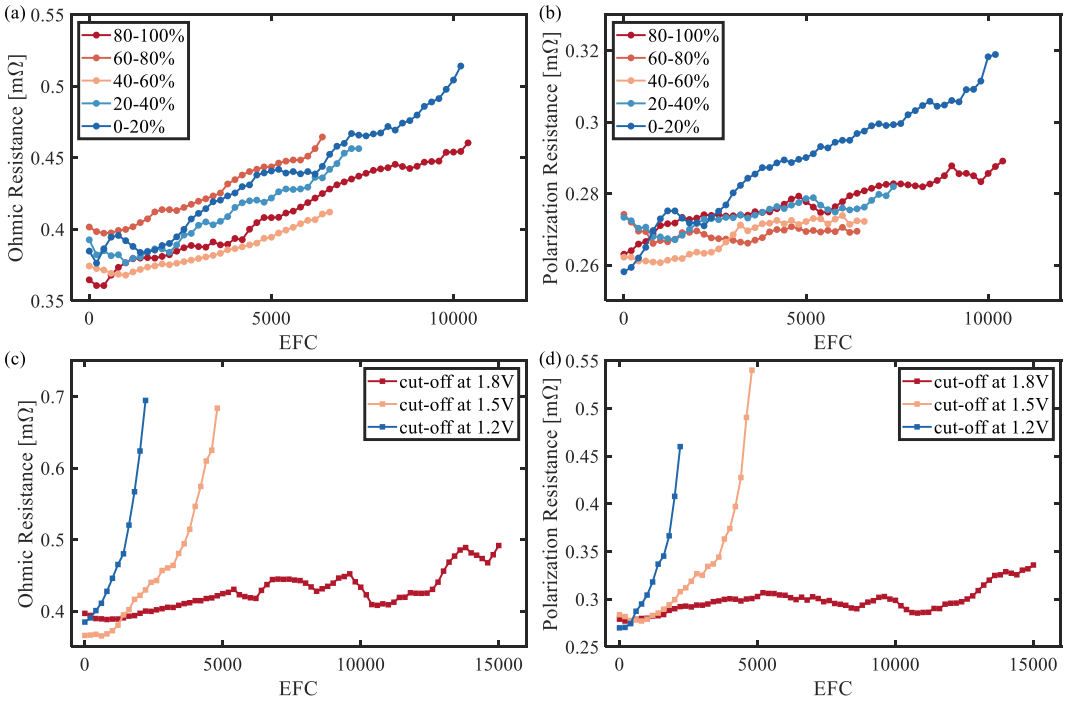

Fig. 12. The ohmic and polarization resistance over equivalent full cycle (EFC) for cells cycled at (a, b) different SOC intervals and (c, d) different discharge cut-off voltages.

$$R_{ohmic} = \frac{\Delta V_{10ms}}{I}$$
$$R_{polarization} = \frac{\Delta V_{10s} - \Delta V_{10ms}}{I} \quad (9)$$

The calculation of the resistance from the HPPC experiments is given in Eq. (9). The response time of the ohmic resistance is very fast and almost instantaneous, whereas the polarization response appears after a few seconds. Therefore, we used the voltage change over 10 ms divided by the current to calculate the ohmic resistance, while the effect of the ohmic resistance was excluded from the calculation of the polarization resistance. All the resistance values are calculated by averaging the values obtained from different SOCs and different charging and discharging directions.

Fig. 12(a) and (b) show that the increase of polarization resistance with cells cycled in the 0–20 % SOC interval is slightly larger than the remaining four SOC intervals. However, the increase in polarization resistance is not significant compared to ohmic resistance. Combined with the results of Fig. 4(c), it shows that the kinetic degradation of the cells cycled at 20 % DOD is not significant. While cycling in the 0–20 % SOC interval slightly accelerates the kinetic degradation.

Fig. 12(c) and (d) show that the resistance increases badly when the cut-off voltage is less than 1.5 V. Furthermore, the increase in resistance is more severe with 1.2 V as the cut-off voltage than with 1.5 V as the cut-off voltage, and this applies to both ohmic resistance and polarization resistance. In contrast, the increase in resistance at a cut-off voltage of 1.8 V is minimal. Combined with the results of Fig. 4(d), it can be concluded that for cells cycled at 100 % DOD, using a cut-off voltage of lower than 1.5 V would result in significant kinetic degradation. It is worth noting that although the final ohmic resistance values are similar for the cells with 1.5 V and 1.2 V cut-off voltages, the cell with 1.2 V cut-off voltage has a lower polarization internal resistance. This indicates that the ohmic resistance is more sensitive to lower cut-off voltages than the polarization resistance in kinetic degradation.

To analyze the mechanism of kinetic degradation at low cut-off voltages, we investigated the EIS for these two cells with cut-off voltages less than 1.5 V. The impedance spectra and calculated DRT for the pristine and aged cells are given in Fig. 13(a–f), respectively. It can be seen that the ohmic resistance of the battery remains unchanged after aging, while the increase in impedance is mainly due to the increase in the semicircle diameter of the intermediate-frequency part and the increase in the diffusive resistance of the low-frequency part. Since the frequency range of the experiment is 0.01 Hz–1000 Hz, corresponding to a time domain range of 10^{-3} - 10^{2} s, the DRT values outside this range (grey parts) are inaccurate and, therefore, not evaluated.

There is only one semicircle is visible at the intermediate frequency of the EIS, while there are three peaks in the corresponding DRT space, which are labeled F1-3 as the time constant increases. In the literature, with increasing time constants, the DRT peaks can be attributed to the contact impedance, lithium-ion transport processes at the SEI/CEI, the charge transfer processes, and the diffusion processes [48–50]. Since the contact impedance is independent of SOC and its time constant is usually less than 10^{-3} s, this process is not included in our DRT plot. Considering that the time constant of the SEI/CEI process is independent of SOC, we attribute the peak F1 to the charge transfer process. Its time constant is too small to be the diffusion process and is highly correlated with the SOC. The peak F2 has a negligible dependence on SOC, but since the time constant of the SEI/CEI is typically less than 10^{-1} s and the time constant of the diffusion process is strongly correlated with SOC, F2 can be attributed to another charge transfer process. Compared to F1, F2 has a larger time constant. Therefore, we attribute F1 to the charge transfer process at the cathode LCO and F2 to the charge transfer process at the anode LTO [51]. F3 has the largest time constant, which can be linked to the diffusion process of the positive or negative electrode, and its exact time constant cannot be identified due to the limitation of the experimental frequency.

Comparing Fig. 13(c) and (d) shows that the impedance at the end of aging for the cell aged at the 1.2 V cut-off voltage is less than that of the 1.5 V cell. This is consistent with the results in Fig. 12(d) and suggests that while a lower cut-off voltage accelerates the cell kinetic degradation, the kinetic performance at the end of aging also depends on the length of the aging process experienced.

It can be observed that the height of F1 in Fig. 13(d–f) is higher than that in Fig. 13(b), indicating an increase in the charge transfer resistance

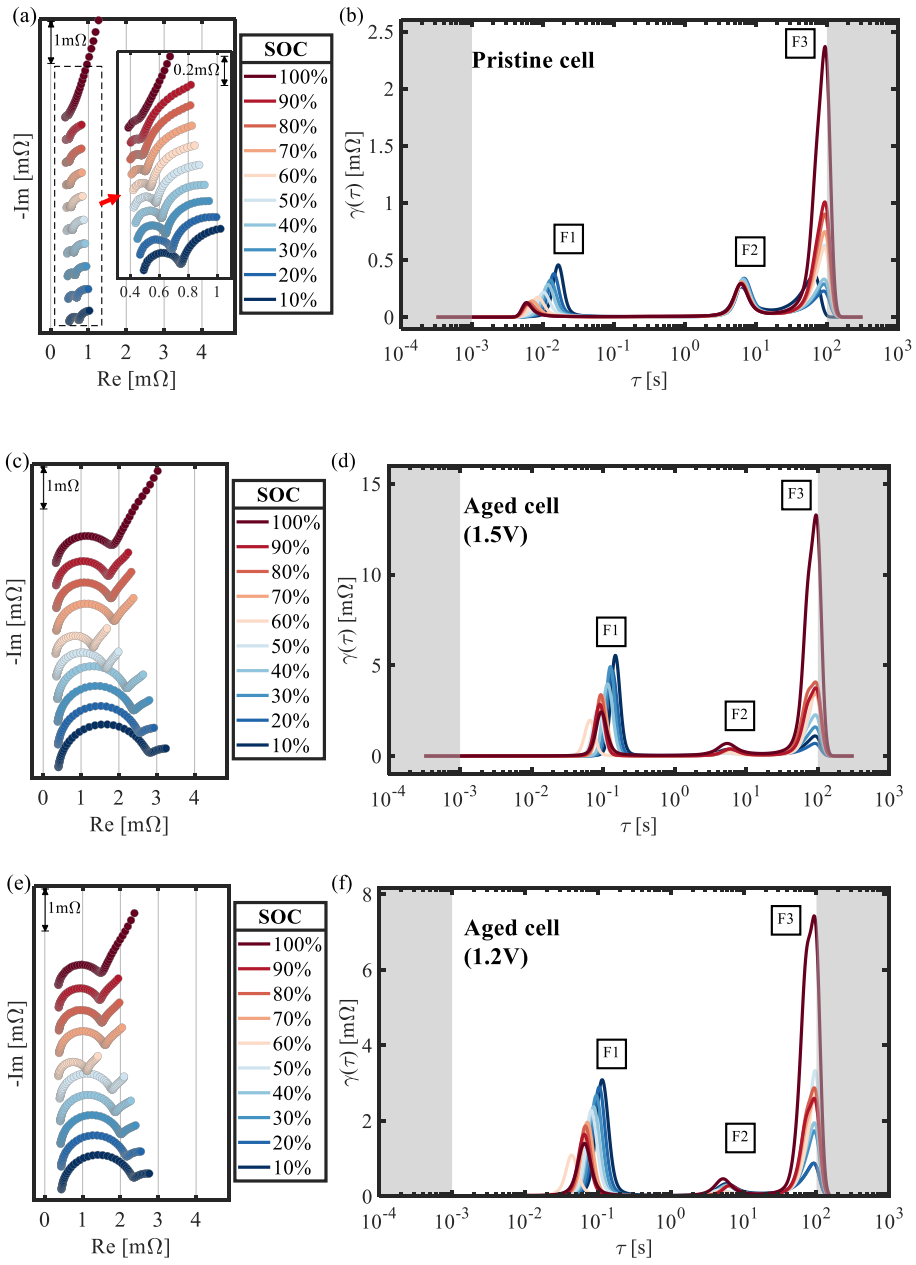

Fig. 13. Impedance spectra and DRT of the pristine and aged cell at 25 °C. Notice: Impedance spectra are shifted in the y-direction for visualization purposes. Grey parts in the DRT plot have not been evaluated.

at the cathode after aging. Nevertheless, the height of F2 is basically unchanged, which means that the resistance at the LTO/electrolyte interphase has not changed significantly over aging, again proving the previously mentioned advantage of no SEI formation for LTO anodes [52].

For the pristine cell, the height of F1 decreases as the SOC increases. However, for the aged battery, the height of F1 decreases with increasing SOC up until 60 % SOC. Afterward, the height of F1 starts to increase between 70–100 % SOC. Therefore, the minimum value of the impedance was found at 60 % SOC in the aged battery. This behavior can be attributed to the fact that the charge transfer impedance of Li_xCoO_2 shows a minimum at the two-phase transition region where $x = 0.9$ and maxima at high and low SOC [48,49]. Generally, Li_xCoO_2 materials are designed to work in the range of $x > 0.5$ to ensure a long cycle life [53]. During the charging process corresponding to x from 1 to 0.5, the Li_xCoO_2 material undergoes a continuous phase transition between the insulating, metallic and monoclinic phases [35]. Where charge transfer impedance of Li_xCoO_2 shows a minimum at the insulating/metal transition region. Usually, the capacity of the cathode material is oversized for batteries with LTO anode. As a result, the cathode of a pristine battery remains within the two-phase transition region when the full cell is fully discharged. However, the positive active material decreases during aging, accompanied by changes in the lattice structure, resulting in an operating range outside the two-phase transition region. Therefore, the observed semicircle in the impedance measurements increases at low SOCs.

Furthermore, the low-frequency part of the impedance spectrum is approximately a straight line for the aged cell at high SOC intervals. Meanwhile, in low SOC intervals, the low-frequency part of the impedance spectrum gets bent toward the x-axis. This is because the anode charge transfer impedance and the diffusion impedance have similar frequencies and substantially the same magnitude at low SOCs, which makes the shape of the low-frequency impedance similar to a half circle. At high SOCs, the diffusion impedance is much larger than the

impedance of the anode charge transfer process. Therefore, the low-frequency part of the impedance spectrum converges into a straight line with an angle of 45° relative to the x-axis.

The DRT analysis results for the impedance spectra of pristine and aged batteries at different temperatures are shown in Fig. 14. For both pristine and aged batteries, the height and the time constants of F1 and F2 increase with decreasing temperature. This reflects that the charge transfer process is decelerated at low temperatures, which is equivalent to an increase in the charge transfer impedance. Since the anode LTO material is less affected by temperature than the cathode LCO material, the height and time constant of F2 change less with temperature compared to F1, further confirming our previous analysis. In addition, the small height of F3 at 0 °C may be because its time constant at this temperature is much larger than 10^2 s. Only part of its peak is identified, and the maximum of its height is not reached. In contrast, F3 at 25 °C has a shorter time constant, making it closer to its maximum height at 10^2 s. Therefore, the height of F3 at 25 °C is greater than the height at 0 °C.

To double-check the DRT results, we chose three circuits with a parallel connection of resistor R and constant phase element (CPE) to fit the EIS results since there are three peaks in Fig. 13(a). In addition, an inductive circuit consisting of R and L in parallel was added to fit the high-frequency (>1000 Hz) part of the EIS. R_0 represents the ohmic resistance of the battery. R_1 and CPE_1 represent the cathode charge transfer process corresponding to F1 in the DRT, whereas R_2 and CPE_2 represent the anode charge transfer process corresponding to F2 in the DRT. Furthermore, R_3 and CPE_3 represent the diffusion process. Considering that the inductive part of the impedance is too small and that the diffusion part is only partly identified. The comparative analysis was performed only for the charge transfer process at the cathode and anode.

The time constant of each process obtained from the equivalent circuit can be calculated by Eq. (10)

$$\tau_n = R_n \cdot CPE_n \tag{10}$$

Where τ_n is the time constant, R_n and CPE_n are the impedance of the corresponding process and the capacitance of the constant-phase element, respectively. The comparison between the fitted model parameter values of τ_n and the time constants of F1 and F2 obtained from the DRT are shown in Fig. 15. The time constants obtained from the EC and DRT are shown in Fig. 15(b and c). To verify the accuracy of the double-check, the error metrics used are defined as follows: where y and $\tilde{y}$ are the actual and estimated values, respectively, and n denotes the different SOCs. We select the value obtained from EC as the actual value and the value obtained from DRT as the estimated value. There are two

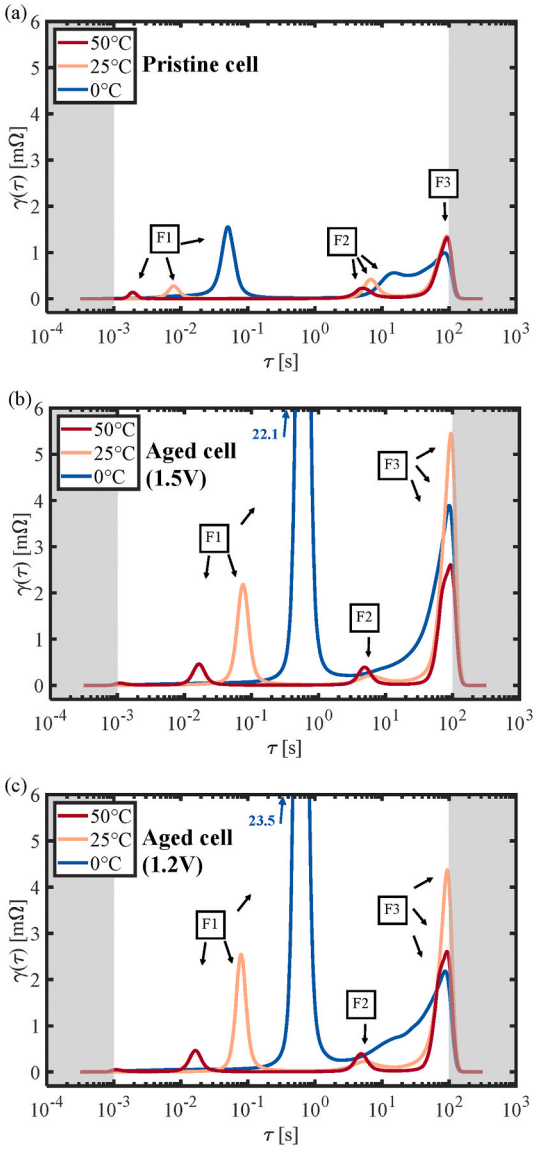

Fig. 14. DRT of pristine aged cells at 50 % SOC under different temperatures. Notices: Grey parts in the DRT plot have not been evaluated.

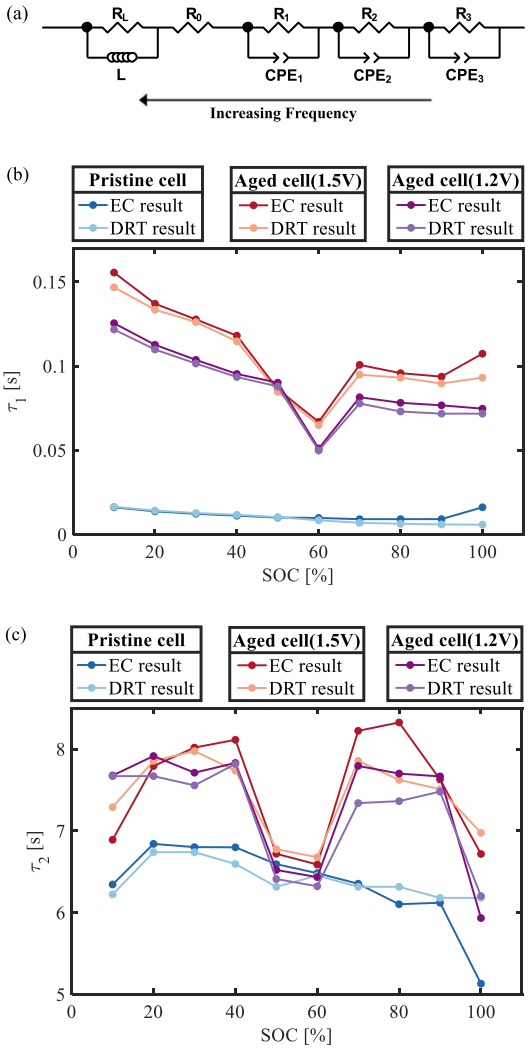

Fig. 15. (a) The equivalent circuit models used to fit the impedance spectra. Comparison plots for time constants obtained from EC and DRT at different SOCs at 25 °C for (b) τ_1 and (c) τ_2.

important evaluation metrics, which are the mean absolute error (MAE) score and the mean absolute percentage error (MAPE) score. The formulas for calculating the MAE and MAPE scores are given in Eqs. (11) and (12), respectively.

$$\mathrm{MAE} = \frac{\sum_{i=1}^{n} |y_i - \widetilde{y}_i|}{n} \tag{11}$$

$$\mathrm{MAPE} = \frac{\sum_{i=1}^{n} \left| \frac{y_i - \widetilde{y}_i}{y_i} \right|}{n} \tag{12}$$

Both scores indicate better accuracy with lower values, and the results are shown in Table 3, where the mean value is calculated by Eq. (13) below.

$$\mathit{Mean\ value} = \frac{\sum_{i=1}^{n} \left(\frac{y_i - \widetilde{y}_i}{2} \right)}{n} \tag{13}$$

As shown in Table 3, the MAPE for all time constants is less than 5 %, except for τ_1 for the pristine cell. This is due to the small value of the pristine τ_1. Even though the absolute error is small, it still results in a large MAPE compared to the original value.

After the double validation of EC and DRT, the obtained time constants can be quantitatively analyzed to understand the kinetic degradation mechanisms of the battery. Compared to the pristine cell, the aged τ_1 increased by 887 % and 791 % for 1.5 V and 1.2 V cut-off voltages, respectively. The rapid increase of τ_1 may be due to the deterioration of the aged LCO electrode structure, such as particle cracking, thickening of the CEI, etc., which makes the charge transfer more difficult [54,55]. It is worth noting that τ_1 is smaller for cells with a 1.2 V cut-off voltage than that with a 1.5 V cut-off voltage. This is consistent with the previous conclusion that polarization resistance is less sensitive to the lower cut-off voltages than ohmic resistance.

The time constant τ_2 of the anode increased by only 17 % and 14 % for the 1.5 V and 1.2 V cut-off voltages. Compared to the large increase in cathode τ_1, the change in time constant τ_2 for the anode is much smaller. This suggests that the increase in polarization resistance triggered by the lower cut-off voltage in the kinetic degradation of the LTO battery mainly originates from the slowing down of the cathode charge transfer process.

In general, the kinetic degradation of the cells cycled at 20 % DOD was not significant, and only a slight increase in polarization resistance was observed for the cell cycle in the 0–20 % SOC interval. In contrast, cells cycling at 100 % DOD showed a significant kinetic degradation if the cut-off voltage was less than 1.5 V. The main mechanism for the kinetic degradation of the LTO cells is the slowing down of the charge transfer process and the diffusion process of the cathode. The LTO anode remains essentially unchanged during cyclic aging and does not affect the kinetic performance of the battery.

4. Conclusion

This work presents and discusses the cyclic aging behavior of LTO cells cycled at five different SOC intervals at 20 % DOD and three different discharge cut-off conditions at 100 % DOD. The aging mechanisms of the cells under different conditions can be divided into thermodynamic degradation and kinetic degradation. The thermodynamic degradation was analyzed using DVA and OCV reconstruction methods. Kinetic degradation was analyzed using EIS combined with DRT. The main conclusions are summarized:

1) The thermodynamic and kinetic performance of LTO batteries exhibits slower degradation when cycled at 20 % DOD compared to cycling at 100 % DOD. Cycling at 20 % DOD shows that the best battery life is achieved during high SOC intervals. Additionally, maintaining a cut-off voltage above 1.8 V during 100 % DOD cycling can significantly enhance the battery's lifespan.
2) Lowering the discharge cut-off voltage accelerates both thermodynamic and kinetic degradation, with a more pronounced effect on kinetic degradation. For batteries with different cut-off voltages reaching the end-of-life, the reduction of cut-off voltage from 1.8 V to 1.2 V resulted in an increase in the percentage of kinetic loss from 16.7 % to 73.4 %.
3) $\mathrm{LAM_{cat}}$ is the degradation mode that has the most significant impact on thermodynamic performance, contributing to over 50 % of the total thermodynamic losses. Moreover, the percentage of thermodynamic losses attributed to $\mathrm{LAM_{cat}}$ increases as the cut-off voltage decreases.
4) The capacity recovery effect caused by LLI is highly significant in cells with LTO anodes. For the investigated cells, LLI extends the operating range of the cathode and partially recovers the capacity loss caused by other degradation modes.
5) In contrast to graphite cells, the primary cause of kinetic degradation in LTO cells is attributed to the cathode, specifically the deceleration of the charge transfer and diffusion processes. Conversely, the LTO anode experiences minimal changes during cyclic aging and has a negligible effect on the overall kinetic performance of the cell.

Table 3
Validation results.

	Pristine τ_1	Aged τ_1 (1.5 V)	Aged τ_1 (1.2 V)	Pristine τ_2	Aged τ_2 (1.5 V)	Aged τ_2 (1.2 V)
Mean value [s]	0.011	0.107	0.087	6.382	7.465	7.251
MAE [s]	0.002	0.005	0.003	0.215	0.247	0.189
MAPE [%]	18.2	4.3	3.6	3.7	3.2	2.6

Our results suggest that when applying LTO batteries as power sources, it is better to maintain their operating range in the higher SOC interval. This not only allows more energy due to the higher voltage but also extends the lifespan of the battery. Moreover, it is necessary to ensure that the LTO battery voltage is maintained above 1.8 V, otherwise, accelerated degradation may be triggered.

Our future research will investigate the internal linkage of LTO battery degradation between the five SOC intervals with 20 % DOD and the complete SOC interval with 100 % DOD. Based on the results of that study, we will establish a rapid test method for LTO batteries by using more test channels to perform cyclic aging under the partitioned small SOC intervals to reduce the life test time.

CRediT authorship contribution statement

Haoze Chen: Writing – review & editing, Writing – original draft, Validation, Software, Methodology, Conceptualization. **Ahmed Chahbaz:** Writing – review & editing, Validation, Methodology. **Sijia Yang:** Writing – review & editing, Visualization, Validation. **Weige Zhang:** Supervision, Resources, Funding acquisition. **Dirk Uwe Sauer:** Writing – review & editing, Supervision, Funding acquisition. **Weihan Li:** Writing – review & editing, Supervision, Methodology.

Declaration of competing interest

The authors declare that they have no known competing financial interests or personal relationships that could have appeared to influence the work reported in this paper.

Data availability

Data will be made available on request.

Acknowledgments

This work was supported by the Science and Technology Research and Development Plan Project of China National Railway Group Co., Ltd. (L2022J002) and the Federal Ministry of Education and Research of Germany through the project BALd (BMBF 03XP0320A).

Appendix A. Supplementary data

Supplementary data to this article can be found online at https://doi.org/10.1016/j.etran.2024.100340.

References

[1] Larcher D, Tarascon JM. Towards greener and more sustainable batteries for electrical energy storage. Nat Chem 2015;7:19–29. https://doi.org/10.1038/nchem.2085.
[2] Wegmann R, Döge V, Sauer DU. Assessing the potential of a hybrid battery system to reduce battery aging in an electric vehicle by studying the cycle life of a graphite|NCA high energy and a LTO|metal oxide high power battery cell considering realistic test profiles. Appl Energy 2018;226:197–212. https://doi.org/10.1016/j.apenergy.2018.05.104.
[3] Cicconi P, Postacchini L, Pallotta E, Monteriù A, Prist M, Bevilacqua M, et al. A life cycle costing of compacted lithium titanium oxide batteries for industrial applications. J Power Sources 2019;436:226837. https://doi.org/10.1016/j.jpowsour.2019.226837.
[4] Farmann A, Waag W, Sauer DU. Application-specific electrical characterization of high power batteries with lithium titanate anodes for electric vehicles. Energy 2016;112:294–306. https://doi.org/10.1016/j.energy.2016.06.088.
[5] Herrera VI, Gaztañaga H, Milo A, Saez-De-Ibarra A, Etxeberria-Otadui I, Nieva T. Optimal energy management and sizing of a battery-supercapacitor-based light rail vehicle with a multiobjective approach. IEEE Trans Ind Appl 2016;52:3367–77. https://doi.org/10.1109/TIA.2016.2555790.
[6] Chahbaz A, Meishner F, Li W, Ünlübayir C, Uwe Sauer D. Non-invasive identification of calendar and cyclic ageing mechanisms for lithium-titanate-oxide batteries. Energy Storage Mater 2021;42:794–805. https://doi.org/10.1016/j.ensm.2021.08.025.
[7] Schröer P, Khoshbakht E, Nemeth T, Kuipers M, Zappen H, Sauer DU. Adaptive modeling in the frequency and time domain of high-power lithium titanate oxide cells in battery management systems. J Energy Storage 2020;32. https://doi.org/10.1016/j.est.2020.101966.
[8] Wang G, Kong D, Ping P, Wen J, He X, Zhao H, et al. Revealing particle venting of lithium-ion batteries during thermal runaway: a multi-scale model toward multiphase process. eTransportation 2023;16. https://doi.org/10.1016/j.etran.2023.100237.
[9] Han X, Lu L, Zheng Y, Feng X, Li Z, Li J, et al. A review on the key issues of the lithium ion battery degradation among the whole life cycle. eTransportation 2019;1:100005. https://doi.org/10.1016/j.etran.2019.100005.
[10] Bank T, Alsheimer L, Löffler N, Uwe D. State of charge dependent degradation effects of lithium titanate oxide batteries at elevated temperatures : an in-situ and ex-situ analysis. J Energy Storage 2022;51:104201. https://doi.org/10.1016/j.est.2022.104201.
[11] Bank T, Feldmann J, Klamor S, Bihn S, Sauer DU. Extensive aging analysis of high-power lithium titanate oxide batteries: impact of the passive electrode effect. J Power Sources 2020;473:228566. https://doi.org/10.1016/j.jpowsour.2020.228566.
[12] Zhang L, Zhang S, Zhou Q, Snyder K, Miller T. Electrolytic solvent effects on the gassing behavior in LCO||LTO batteries. Electrochim Acta 2018;274:170–6. https://doi.org/10.1016/j.electacta.2018.04.113.
[13] Devie A, Dubarry M, Liaw BY. Overcharge study in Li4Ti5O12 based lithium-ion pouch cell I. Quantitative diagnosis of degradation modes. J Electrochem Soc 2015;162:A1033–40. https://doi.org/10.1149/2.0941506jes.
[14] Devie A, Dubarry M, Liaw BY. Overcharge study in Li4Ti5O12 based lithium-ion pouch cell II. Experimental investigation of the degradation mechanism. J Electrochem Soc 2016;163:A2611–7. https://doi.org/10.1149/2.0491613jes.
[15] Liu S, Winter M, Lewerenz M, Becker J, Sauer DU, Ma Z, et al. Analysis of cyclic aging performance of commercial Li4Ti5O12-based batteries at room temperature. Energy 2019;173:1041–53. https://doi.org/10.1016/j.energy.2019.02.150.
[16] Dubarry M, Devie A. Battery durability and reliability under electric utility grid operations: representative usage aging and calendar aging. J Energy Storage 2018;18:185–95. https://doi.org/10.1016/j.est.2018.04.004.
[17] Baure G, Dubarry M. Battery durability and reliability under electric utility grid operations: 20-year forecast under different grid applications. J Energy Storage 2020;29:101391. https://doi.org/10.1016/j.est.2020.101391.
[18] Cipek M, Pavković D, Kljaić Z, Mlinarić TJ. Assessment of battery-hybrid diesel-electric locomotive fuel savings and emission reduction potentials based on a realistic mountainous rail route. Energy 2019;173:1154–71. https://doi.org/10.1016/j.energy.2019.02.144.
[19] Meinert M, Melzer M, Kamburow C, Palacin R, Leska M, Aschemann H. Benefits of hybridisation of diesel driven rail vehicles: energy management strategies and life-cycle costs appraisal. Appl Energy 2015;157:897–904. https://doi.org/10.1016/j.apenergy.2015.05.051.
[20] Wu C, Lu S, Xue F, Jiang L, Chen M. Optimal sizing of onboard energy storage devices for electrified Railway systems. IEEE Trans Transp Electrif 2020;6:1301–11. https://doi.org/10.1109/TTE.2020.2996362.
[21] Gao Y, Jiang J, Zhang C, Zhang W, Jiang Y. Aging mechanisms under different state-of-charge ranges and the multi-indicators system of state-of-health for lithium-ion battery with Li(NiMnCo)O2 cathode. J Power Sources 2018;400:641–51. https://doi.org/10.1016/j.jpowsour.2018.07.018.
[22] An F, Jiang J, Zhang W, Zhang C, Fan X. State of energy estimation for lithium-ion battery pack via prediction in electric vehicle applications. IEEE Trans Veh Technol 2022;71:184–95. https://doi.org/10.1109/TVT.2021.3125194.
[23] Zheng F, Jiang J, Sun B, Zhang W, Pecht M. Temperature dependent power capability estimation of lithium-ion batteries for hybrid electric vehicles. Energy 2016;113:64–75. https://doi.org/10.1016/j.energy.2016.06.010.
[24] Jiang J, Liu S, Ma Z, Wang LY, Wu K. Butler-Volmer equation-based model and its implementation on state of power prediction of high-power lithium titanate batteries considering temperature effects. Energy 2016;117:58–72. https://doi.org/10.1016/j.energy.2016.10.087.
[25] Chen Z, Gu H, Shen S, Shen J. Energy management strategy for power-split plug-in hybrid electric vehicle based on MPC and double Q-learning. Energy 2022;245:123182. https://doi.org/10.1016/j.energy.2022.123182.
[26] Menale C, Constà S, Sglavo V, Della Seta L, Bubbico R. Experimental investigation of overdischarge effects on commercial Li-ion cells. Energies 2022;15. https://doi.org/10.3390/en15228440.
[27] Jung SK, Hwang I, Chang D, Park KY, Kim SJ, Seong WM, et al. Nanoscale phenomena in lithium-ion batteries. Chem Rev 2020;120:6684–737. https://doi.org/10.1021/acs.chemrev.9b00405.
[28] Wang F, Lin Z, Liu L, Wei X, Lin S, Dai L, et al. Does polarization increase lead to capacity fade? J Electrochem Soc 2020;167:090549. https://doi.org/10.1149/1945-7111/ab956b.
[29] Schindler S, Danzer MA. A novel mechanistic modeling framework for analysis of electrode balancing and degradation modes in commercial lithium-ion cells. J Power Sources 2017;343:226–36. https://doi.org/10.1016/j.jpowsour.2017.01.026.
[30] Madej E, Klink S, Schuhmann W, Ventosa E, La Mantia F. Effect of the specific surface area on thermodynamic and kinetic properties of nanoparticle anatase TiO2 in lithium-ion batteries. J Power Sources 2015;297:140–8. https://doi.org/10.1016/j.jpowsour.2015.07.079.
[31] Li S, Li K, Zheng J, Zhang Q, Wei B, Lu X. Structural distortion-induced charge gradient distribution of Co ions in delithiated LiCoO2 cathode. J Phys Chem Lett 2019;10:7537–46. https://doi.org/10.1021/acs.jpclett.9b02711.
[32] Wang Y, Zhang C, Hu J, Zhang P, Zhang L, Lao L. Investigation on calendar experiment and failure mechanism of lithium-ion battery electrolyte leakage. J Energy Storage 2022;54:105286. https://doi.org/10.1016/j.est.2022.105286.
[33] Dubarry M, Truchot C, Liaw BY. Synthesize battery degradation modes via a diagnostic and prognostic model. J Power Sources 2012;219:204–16. https://doi.org/10.1016/j.jpowsour.2012.07.016.
[34] Lewerenz M, Marongiu A, Warnecke A, Sauer DU. Differential voltage analysis as a tool for analyzing inhomogeneous aging: a case study for LiFePO4|Graphite cylindrical cells. J Power Sources 2017;368:57–67. https://doi.org/10.1016/j.jpowsour.2017.09.059.
[35] Lu X, Sun Y, Jian Z, He X, Gu L, Hu YS, et al. New insight into the atomic structure of electrochemically delithiated O3-Li(1- x)CoO2 ($0 \leq x \leq 0.5$) nanoparticles. Nano Lett 2012;12:6192–7. https://doi.org/10.1021/nl303036e.
[36] Reimers JN, Soc JRDJE. Electrochemical and in situ X-ray diffraction studies of lithium intercalation in LixCo02. 1992.
[37] Shao-Horn Y, Levasseur S, Weill F, Delmas C. Probing lithium and vacancy ordering in O3 layered LixCoO2 (x≈0.5). J Electrochem Soc 2003;150:A366. https://doi.org/10.1149/1.1553787.
[38] Minato T, Kawaura H, Hirayama M, Taminato S, Suzuki K, Yamada NL, et al. Dynamic behavior at the interface between lithium cobalt oxide and an organic electrolyte monitored by neutron reflectivity measurements. J Phys Chem C 2016;120:20082–8. https://doi.org/10.1021/acs.jpcc.6b02523.
[39] Zhang JN, Li Q, Wang Y, Zheng J, Yu X, Li H. Dynamic evolution of cathode electrolyte interphase (CEI) on high voltage LiCoO2 cathode and its interaction with Li anode. Energy Storage Mater 2018;14:1–7. https://doi.org/10.1016/j.ensm.2018.02.016.
[40] Chauque S, Oliva FY, Visintin A, Barraco D, Leiva EPM, Cámara OR. Lithium titanate as anode material for lithium ion batteries : synthesis , post- treatment and its electrochemical response. J Electroanal Chem 2017;799:142–55. https://doi.org/10.1016/j.jelechem.2017.05.052.
[41] He YB, Liu M, Huang ZD, Zhang B, Yu Y, Li B, et al. Effect of solid electrolyte interface (SEI) film on cyclic performance of Li4Ti5O12 anodes for Li ion batteries. J Power Sources 2013;239:269–76. https://doi.org/10.1016/j.jpowsour.2013.03.141.
[42] Charles-Blin Y, Flahaut D, Guérin K, Dubois M, Monconduit L, Louvain N, et al. Surface atomic layer fluorination of Li4Ti5O12: investigation of the surface electrode reactivity and the outgassing behavior in LiBs. Appl Surf Sci 2020;527:146834. https://doi.org/10.1016/j.apsusc.2020.146834.
[43] Lewerenz M, Fuchs G, Becker L, Sauer DU. Irreversible calendar aging and quantification of the reversible capacity loss caused by anode overhang. J Energy Storage 2018;18:149–59. https://doi.org/10.1016/j.est.2018.04.029.
[44] Nelson Weker J, Wise AM, Lim K, Shyam B, Toney MF. Operando spectroscopic microscopy of LiCoO2 cathodes outside standard operating potentials. Electrochim Acta 2017;247:977–82. https://doi.org/10.1016/j.electacta.2017.06.173.

[45] Birkl CR, Roberts MR, McTurk E, Bruce PG, Howey DA. Degradation diagnostics for lithium ion cells. J Power Sources 2017;341:373–86. https://doi.org/10.1016/j.jpowsour.2016.12.011.
[46] Pinson MB, Bazant MZ. Theory of SEI formation in rechargeable batteries: capacity fade, accelerated aging and lifetime prediction. J Electrochem Soc 2013;160:A243–50. https://doi.org/10.1149/2.044302jes.
[47] Saccoccio M, Wan TH, Chen C, Ciucci F. Optimal regularization in distribution of relaxation times applied to electrochemical impedance spectroscopy: ridge and Lasso regression methods - a theoretical and experimental Study. Electrochim Acta 2014;147:470–82. https://doi.org/10.1016/j.electacta.2014.09.058.
[48] Shafiei Sabet P, Stahl G, Sauer DU. Non-invasive investigation of predominant processes in the impedance spectra of high energy lithium-ion batteries with nickel–cobalt–aluminum cathodes. J Power Sources 2020;472:228189. https://doi.org/10.1016/j.jpowsour.2020.228189.
[49] Dollé M, Orsini F, Gozdz AS, Tarascon J-M. Development of reliable three-electrode impedance measurements in plastic Li-ion batteries. J Electrochem Soc 2001;148:A851. https://doi.org/10.1149/1.1381071.
[50] Moazzen E, Scipioni R, Ma M, Barnett S. Interpretation and modelling of the electrochemical impedance of LiFePO4/Li4Ti5O12 batteries. J Electrochem Soc 2021;168:050519. https://doi.org/10.1149/1945-7111/abf9c1.
[51] Schweikert N, Heinzmann R, Eichhöfer A, Hahn H, Indris S. Electrochemical impedance spectroscopy of Li4Ti5O12 and LiCoO2 based half-cells and Li4Ti5O12/LiCoO2 cells: internal interfaces and influence of state-of-charge and cycle number. Solid State Ionics 2012;226:15–23. https://doi.org/10.1016/j.ssi.2012.08.002.
[52] Hall F, Touzri J, Wußler S, Buqa H, Bessler WG. Experimental investigation of the thermal and cycling behavior of a lithium titanate-based lithium-ion pouch cell. J Energy Storage 2018;17:109–17. https://doi.org/10.1016/j.est.2018.02.012.
[53] Wang X, Wang X, Lu Y. Realizing high voltage lithium cobalt oxide in lithium-ion batteries. Ind Eng Chem Res 2019;58:10119–39. https://doi.org/10.1021/acs.iecr.9b01236.
[54] Guan T, Zuo P, Sun S, Du C, Zhang L, Cui Y, et al. Degradation mechanism of LiCoO2/mesocarbon microbeads battery based on accelerated aging tests. J Power Sources 2014;268:816–23. https://doi.org/10.1016/j.jpowsour.2014.06.113.
[55] Wang K, Wan J, Xiang Y, Zhu J, Leng Q, Wang M, et al. Recent advances and historical developments of high voltage lithium cobalt oxide materials for rechargeable Li-ion batteries. J Power Sources 2020;460:228062. https://doi.org/10.1016/j.jpowsour.2020.228062.